UNIVERSITY OF MONS

FACULTY OF SCIENCE

Master's thesis

Towards Enhanced Monte Carlo Simulation of Extremely-High Energy Neutrinos in the IceCube Experiment via Deep Learning Techniques

Thomas Delmeulle

Department of Physics
Research unit: Inter-University Institute For High Energies

Supervisors: Dr. Simona Toscano
Dr. Felix Schlüter
Dr. Evelyne Daubie

« L'auteur, DELMEULLE THOMAS, atteste avoir respecté les règles éthiques en vigueur, y compris la charte de l'Université relative à l'utilisation de l'Intelligence Artificielle ».

Academic year: 2023–2024

Acknowledgements

First of all, I would like to thank Dr. Simona Toscano, one of the supervisors of this thesis, for allowing me to carry out this work within the IceCube international collaboration. But above all I would like to thank her for her availability and exceptional teaching qualities, as well as for the warm welcome and support I received throughout the year. I also thank Dr. Felix Schlüter for guiding me towards this research topic, for his infinite patience with my level of English and computer skills, and for his remarkable availability. I am grateful to Dr. Evelyne Daubie for allowing me to undertake this thesis within a department outside of UMons and for her guidance, support, and unwavering confidence during difficult times.

I would also like to thank my brothers, Guillaume and Matthieu, and my sister, Aude, for supporting me not only during this final year of study but also throughout the previous four years. Added to these thanks, Nicolas Maindiaux, Elodie Tonnoir, Maud Balcaen, William Delplanque, Sebastien Gamrath for their support, the discussions and all the moments of relaxation which allowed me to complete this work. A special thanks to Laura for listening without understanding, supporting without complaining, and accompanying me during difficult times.

Finally, I thank my parents, Nathalie and Pierre, from the bottom of my heart. Without them, it would have been impossible for me to obtain a Master's degree in Physics. I am deeply grateful for everything they have done for me, both during my studies and beyond. Lastly, I thank my grandfather, Jean, this teacher, for the great lesson he taught me this year.

Abstract

The IceCube Neutrino Observatory was constructed to detect astrophysical neutrinos. It uses the Cherenkov light produced by secondary particles resulting from a neutrino interaction with an ice nucleus, to detect the passage of these elusive particles. However, identifying extremely high-energy neutrinos within the vast amount of collected data requires efficient, robust, and precise analysis methods. With the development of deep learning in recent years, new simulation and reconstruction techniques, using neural networks, have been developed by the IceCube collaboration.

This work evaluates the validity of using one of these new reconstruction methods, based on a convolutional neural network and named Event-Generator, to simulate the temporal distribution and the number of Cherenkov photons reaching each optical module for cascade events.

For this research, the neural network has been retrained to enhance its predictions. The new model successfully predicts the expected amount of light and accounts for light propagation effects in the presence of the dust layer. This result shows that the use of this simulation method is promising with lots of room for improvement.

Contents

Introduction

For millennia, humans gazed at the heavens, relying solely on visible light for observation, as it was the only perceptible aspect to their eyes. What began as a primarily religious practice evolved into the field of astronomy as the study of the celestial sphere became more systematic. Over several centuries, increasingly sophisticated lenses and telescopes were employed to explore the sky. However, in the twentieth century, this scientific domain underwent a profound transformation due to the advancements in modern physics. New methodologies emerged, grounded in the examination of cosmic rays, gamma rays, neutrinos, and more recently, gravitational waves, supplementing the traditional analysis of optical photons. This led to the establishment of significant terrestrial detectors such as LIGO [1] and Virgo [2] for gravitational waves, IceCube [3], ANTARES [4], and the Pierre Auger Cosmic Ray Observatory [5] for neutrinos and cosmic rays, alongside orbiting detectors like the Fermi [6] satellite for gamma rays. The pooling of data from these diverse detectors heralded the emergence of a new discipline: multimessenger astronomy.

Among these diverse sources of information, neutrinos stand out due to their ability to interact solely via weak interaction. This has several important implications: on the one hand, neutrinos arrive from their production site to earth undeflected, without being absorbed which make they the ideal messenger, and on the other hand, it makes their detection notably challenging and necessitating the development of increasingly sophisticated detectors. The IceCube Neutrino Observatory, deployed between 2004 and 2010 in the ice of Antarctica, was established to detect astrophysical neutrinos. In 2013, the discovery of the highest-energy neutrinos ever detected was officially announced. Their energies ranging from tens of TeV to a few PeV suggest an origin beyond the solar system [7]. Since then, other detections have taken place and the analysis of the data has made it possible to identify individual sources of astrophysical neutrinos such as the blazar TXS 0506+056 [8], the nearby active galaxy NGC 1068 [9] and even the galactic plane [10].

Beyond PeV energies, an additional component to the observed astrophysical flux is believed to arise from the interaction of the ultra-high-energy cosmic rays (UHECRs) with the background photon field in the universe (cosmogenic neutrinos). These extremely-high-energy (EHE) neutrinos carry important information about the origin of UHECRs but are, as of now, still undetected. Recently, IceCube has published the most stringent upper limit on the EHE neutrino flux using more than 12 years of data.

The research presented in this thesis is part of a broader endeavor to develop the next-generation EHE analysis in IceCube, with a particular focus on improving sensitivity in the energy region where the transition between the astrophysical and cosmogenic components occurs. To achieve this, it is imperative to possess a large quantity of the most faithful simulations possible of events occurring within the detector. Information such as the location, direction, and energy of the particles traversing it is deduced from the collected Cherenkov light signature. One of the main aspects of these simulations lies in reproducing the amount of light recorded by IceCube's digital optical modules for

high-energy cascade events. This master's thesis presents an assessment of the reliability of simulating the photon distribution using a new simulation method, Event-Generator [11], developed by the IceCube collaboration. This method, based on the use of a neural network, is compared to another technique, Photonics [12], which has been used for several years and is based on interpolating data tables produced from Monte Carlo simulations. Both methods are then compared to the full MC simulation, for which a full propagation of the produced photons in the ice is performed. However, as the energy of incident neutrinos increases, the number of Cherenkov photons produced grows, and the computational power required for this step becomes significant. Several approximations are made by conventional methods to reduce this cost. Utilizing an efficient and reliable method based on deep learning would enable achieving this objective while reducing the necessary approximations. In this work, the NN-based algorithm has been trained with the purpose of improving predictions on the signal distribution within the detector. The primary criterion used for an initial assessment of the quality of the NN predictions is the comparison of the predicted total charge.

The first chapter of this work begins with a brief description of multi-messenger astronomy. It is followed by a recapitulation of the necessary theoretical principles of neutrino-matter interactions and of cascade events, accompanied a description of the IceCube detector in chapter 2. Next, chapter 3 provides an explanation of the steps involved in simulating an event, along with an introduction to the three methods used to simulate the expected charge produced in each DOMs by the neutrino-induced particle cascade. Comparison of the total collected charge at high and low energies is subsequently presented in chapter 4. This master's thesis concludes with chapter 5, which summarizes the main findings and offers insights into the future of this research work.

Chapter 1

Multimessenger astronomy

During the past century, astronomy and astrophysics have undergone significant transformations in their methodologies. Presently, there exist four distinct messengers utilized for probing the universe within and beyond Earth's vicinity:

- Cosmic Rays, initially proposed by Charles Wilson in 1900 and subsequently detected by Victor Hess during a balloon expedition twelve years later.
- Gamma rays, meticulously scrutinized, particularly through various satellite missions since 1961 [13].
- Gravitational waves, whose detection in 2015 [14] was rendered feasible through Albert Einstein's theory of general relativity.
- Neutrinos, these exceedingly elusive particles conjectured by Pauli in his correspondence with Lise Meitner on December 4, 1930 [15].

1.1 Cosmic Rays

Shortly after their existence was confirmed, cosmic rays underwent meticulous examination. Comprising both primary and secondary components, these rays denote high-energy particles penetrating Earth's atmosphere from space. Primary cosmic rays mainly consits of charged particles: 89% protons, 10% α particles (helium nuclei), and 1% heavy nuclei [16]. The cosmic-ray flux, recorded above the atmosphere, follows a power law:

$$\frac{d\phi}{dE} \propto E^{-\gamma} \tag{1.1.0.1}$$

where γ ranges from approximately $\gamma \approx 2.7$ for the region known as the "knee" to $\gamma \approx 3$ for the high-energy region, termed the "ankle". This parameter is profoundly influenced by the production mechanisms and losses incurred during the particles' journey through space. The energy spectrum of cosmic rays is shown on Figure 1.1.

These cosmic rays are produced by various sources. At low energies (< 10 GeV), cosmic rays predominantly originate from the Sun. Up to the knee, cosmic rays are composed mainly of protons of galactic origin. The primary contributors to Galactic cosmic rays are supernova remnants [18], although they can also arise from magnetars or micro-quasars. The knne is the region in which a

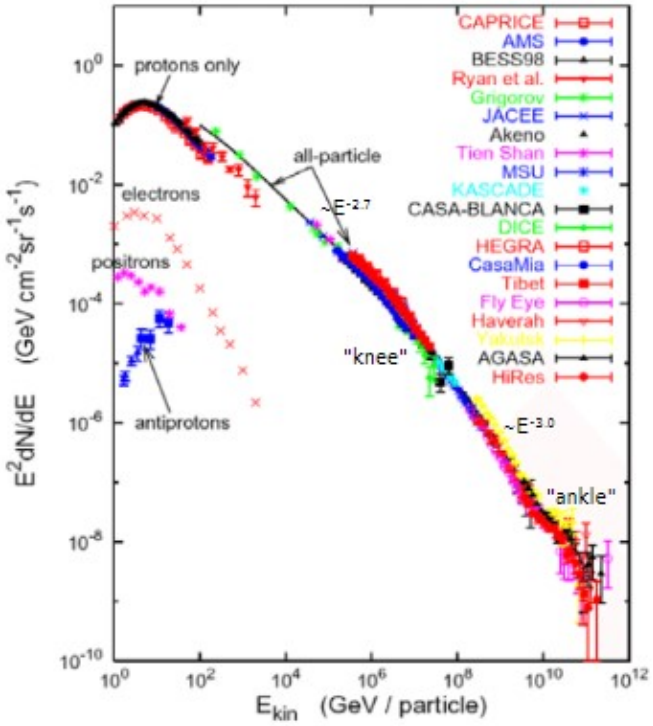

Figure 1.1: Energy spectrum of the primary cosmic ray flux [17].

transition appears in the composition of cosmic rays. Each element would break at different energies toward other elements with lower atomic number Z, the last being iron. Finally, the ankle makes the link between the end of this galactic component of the spectrum and the extra-galactic one.

The spectrum breaks abruptly near energies above 10^{19} eV, a phenomenon known as the GZK cutoff. Discovered by K. Greisen [19] and independently by G. T. Zatsepin and V. A. Kuzmin [20] in 1966, this occurrence is attributed to the interaction between ultra-high-energy cosmic rays (UHECRs) (E $> 10^{19}$ eV) and photons from the cosmic microwave background (CMB). Assuming that UHECRs are primarily protons, the anticipated reaction involves $\Delta^+(1232)$ resonance production, subsequently leading to pion production [21]:

$$\begin{aligned} p + \gamma \rightarrow \Delta^+ &\rightarrow n + \pi^+ \\ &\rightarrow p + \pi^0 \end{aligned} \tag{1.1.0.2}$$

This process, known as photopion production, is characterized by a pronounced increase in the effective cross section for pion-photon collisions around 1225 MeV, as depicted in Figure 1.2 [22].

In the center of mass frame of the system, assuming a head-on collision ($\cos\theta = 1$), the energy threshold required for this reaction is:

$$E_p = \frac{m_{\pi^0}}{4\epsilon}(2m_p + m_{\pi^0}) \simeq 10^{20} eV \tag{1.1.0.3}$$

where m_p and m_{π^0} denote the masses of proton (p) and neutral pion (π^0) respectively, and the average energy of the CMB is considered to be approximately $\approx 6.34 \times 10^{-4}$eV [23], corresponding to the energy of the observed cutoff.

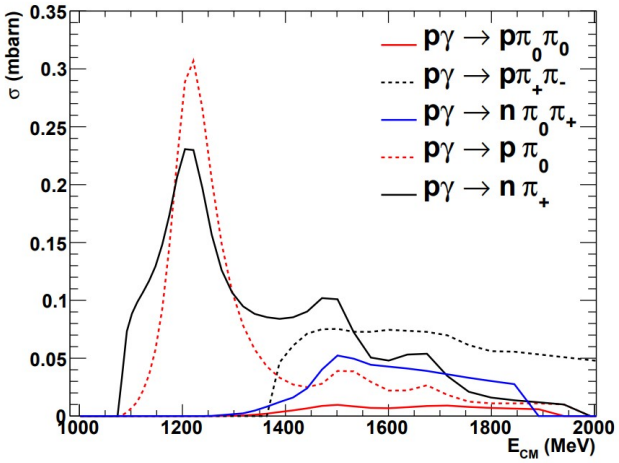

Figure 1.2: Increase in cross sections for photopion production around 1225 MeV, the energy of the Δ^+ resonance [22].

1.1.1 Cosmic-ray induced air showers

Cosmic rays hitting the Earth's atmosphere interact with the atoms in the upper atmosphere, leading to the generation of a lot of new particles constituting secondary cosmic radiation. Subsequently, these secondary particles decay or undergo further interactions with environmental molecules, setting off a cascading effect known as an air shower.

Upon the initial proton's arrival, the most prevalent secondary particles produced are pions (about 90%) and kaons (approximately 10%), forming the hadronic component of the air shower. This cascade of particles originates from the leptonic decay of charged π and K:

$$\pi^+ \to \mu^+ + \nu_\mu \qquad \pi^- \to \mu^- + \bar{\nu}_\mu \tag{1.1.1.1}$$

$$K^+ \to \mu^+ + \nu_\mu \qquad K^- \to \mu^- + \bar{\nu}_\mu \tag{1.1.1.2}$$

Subsequently, the produced muons decay, generating electrons and neutrinos or anti-neutrinos:

$$\mu^+ \to e^+ + \nu_e + \bar{\nu}_\mu \qquad \mu^- \to e^- + \bar{\nu}_e + \nu_\mu \tag{1.1.1.3}$$

Given that muons experience minimal energy loss traversing the atmosphere, they constitute roughly 80% of the charged particles at sea level. Moreover, the hadronic air shower extends laterally due to transverse momentum arising during particle production [24].

Neutral pions (comprising approximately one-third of the created pions) decay into a pair of photons:

$$\pi^0 \to \gamma + \gamma \tag{1.1.1.4}$$

The photons subsequently undergo pair production, generating two electrons. As these electrons propagate, they are deflected by the magnetic field of the nucleus and emits a photon, a process called bremsstrahlung. The repetition of this process initiates an electromagnetic cascade. Its longitudinal development is significantly shorter than that of the hadronic cascade, while its lateral expansion results from multiple diffusions.

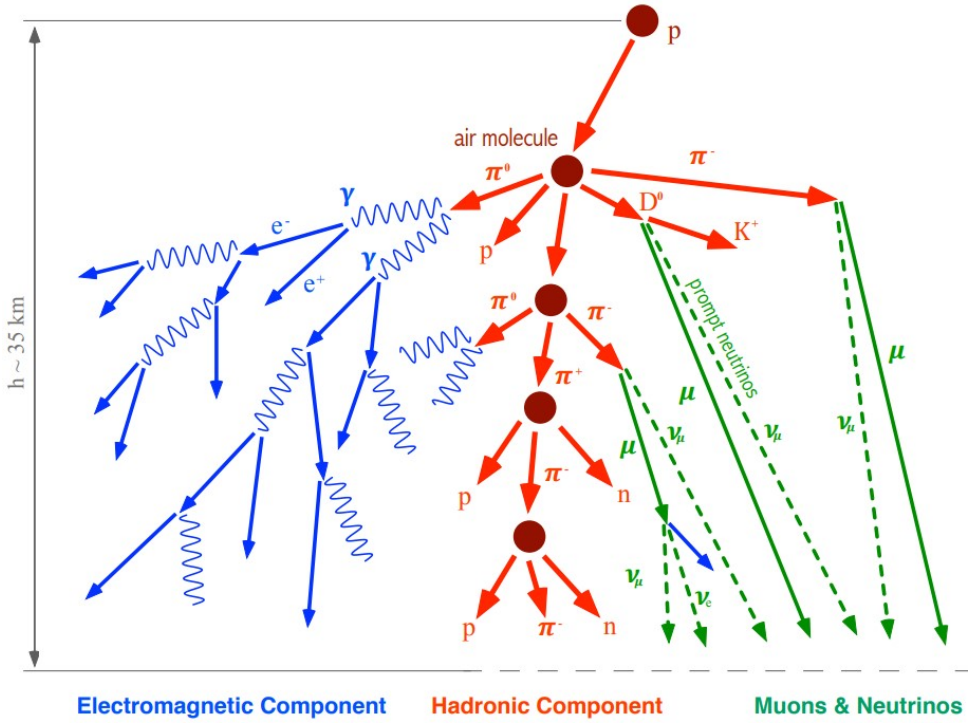

Figure 1.3: Representation of an air shower induced by a high energy incident proton. The three components of the cascade are represented, in blue the electromagnetic part, in red the hadronic part and in green the part containing muons and neutrinos [25].

The only particles capable of penetrating beneath the ground surface are muons and neutrinos due to their low cross section and production altitude, respectively. Consequently, underground muons constitute the primary background for underground neutrino detectors.These three major components of air showers are represented schematically in the Figure 1.3. The electromagnetic part is graphed in blue, the hadronic in red and the muons and neutrinos which result from it in green.

1.2 Gamma rays

As their name suggests, gamma rays consist of gamma photons. Typically, γ photons are defined as having energies ranging from 10^5 eV to 10^{14} eV, with a maximal energy of $\sim$ 100 TeV currently detected for a photon [26]. One major advantage is their exceptional penetrating power as neutral radiation. Consequently, these beams remain unaffected by the magnetic fields permeating the universe, enabling a precise determination of their origin.

Various physical mechanisms contribute to the emission of gamma photons, such as synchrotron radiation, inverse Compton scattering, π_0 decay, or proton synchrotron radiation [27]. Consequently, active galactic nuclei (AGN), particularly blazars, are prominent sources [28]. Gamma radiation also arises from the interaction between the interstellar medium and cosmic rays, leading to the production of numerous pions:

$$p + p \rightarrow p + p + \pi_0 \tag{1.2.0.1}$$

$$\hookrightarrow \pi^0 \rightarrow \gamma + \gamma \tag{1.2.0.2}$$

Nevertheless, gamma-ray astronomy encounters limitations. Firstly, Earth's atmosphere blocks high-energy electromagnetic radiation, including γ-rays. Consequently, to observe them satellites must be deployed outside the atmosphere. Additionally, high-energy photons interact with cosmic microwave background (CMB) photons, resulting in processes such as:

$$\gamma + \gamma \rightarrow e^+ + e^- \text{ or more rarely } \gamma + \gamma \rightarrow \mu^+ + \mu^- \tag{1.2.0.3}$$

This process, therefore, limits the gamma-ray horizon. To provide a sense of scale, for low-energy incident photons (approximately $1\mathrm{TeV}$), the observable distance is around $1\mathrm{Gpc}$. For energies 100 times greater, the distance remains on the order of $1\ \mathrm{Mpc}$. In addition, interactions with particles in the interstellar medium also alter particle energies, causing observed shifts in the energy spectrum [29].

1.3 Gravitational waves

The first direct observation of gravitational waves was made in September 2015 and announced by the LIGO and Virgo collaboration a few months later [30]. Gravitational waves manifest as distortions in the gravitational field that traverse the universe at the speed of light[1].

The sources of gravitational waves currently detectable by ground-based detectors include the inspiral and coalescence of binary systems of compact objects like neutron stars or black holes, the core-collapse of massive stars, and isolated neutron stars [32]. One of the principal advantages of this astrophysical messenger is its exceptionally high propagation speed, which remains largely unaltered even over vast distances. For the events currently observed, the distances range from Mpc to Gpc, depending on the masses of the objects involved [32].

However, the analysis of gravitational wave detection data presents significant uncertainty regarding the direction of arrival of the events. A multi-messenger approach, used to identify (for example) their gamma-ray counterpart in the case of course where the source is considered to be able to emit photons, helps constrain their origin [33].

1.4 Neutrinos

Neutrinos are extremely elusive particles. They are neutral in charge and weakly interacting, allowing them to penetrate the universe largely unaffected by radiation and matter, and remain undeflected by magnetic fields. Leveraging these unique physical properties, scientists can employ neutrinos to probe the inner workings of the astrophysical phenomena under investigation. With few exceptions, such as gravitational waves in certain scenarios [32], neutrinos stand as the sole messengers capable of exploiting this advantage. Consequently, despite the challenges posed by their low interaction cross-section, neutrinos serve as a unique messenger to study high-energy phenomena in the universe.

It has been established that there are three distinct types of neutrinos, each linked to a specific charged lepton. These types are known as "flavors": the tau neutrino, the muon neutrino, and the electron neutrino. As Figure 1.4 shows, they can have a wide range of energies, from $10^{-6}\ \mathrm{eV}$ to $10^{18}\ \mathrm{eV}$. The source of each part of the spectrum is indicated on the graph.

[1] According to general relativity, the speed of propagation of gravitational waves equals the speed of light. Any future experimental findings contradicting this would starkly challenge the theory of general relativity [31].

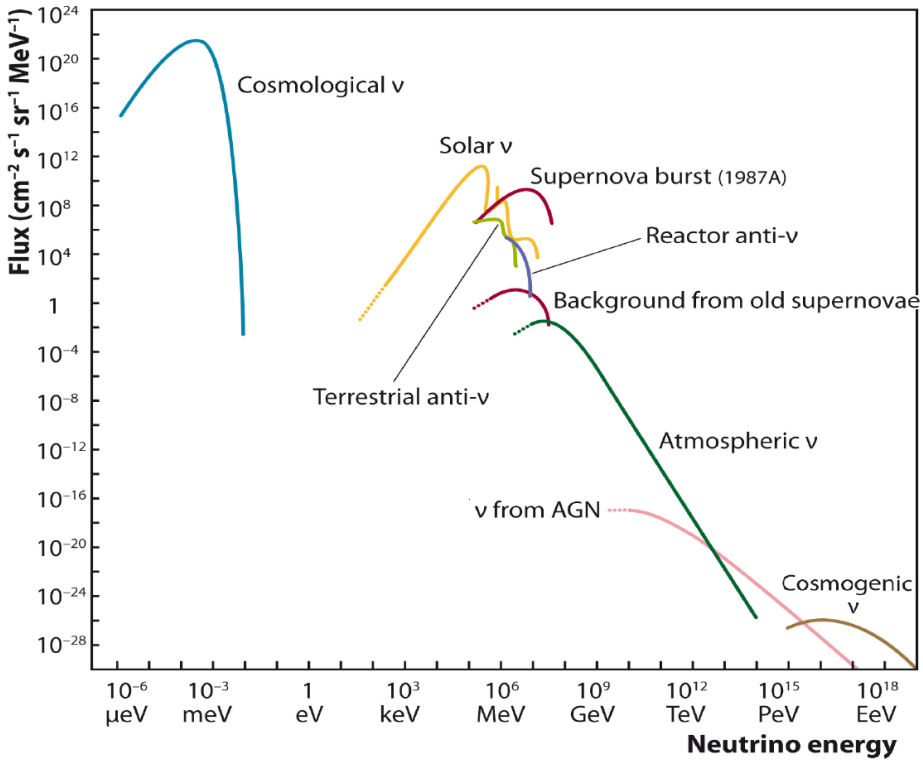

Figure 1.4: Neutrino flux where each part of the spectrum is associated with its origin, including natural sources and reactors [34].

This work focuses on extremely-high-energy (EHE) neutrinos, i.e., $E > 1\mathrm{PeV}$. Generating such energetic particles requires exceptionally powerful astrophysical environments. Several potential astrophysical sources have been proposed. Among them are gamma-ray bursts [35] and Active Galactic Nuclei [36]. These particles are produced when a large number of highly accelerated hadrons encounter matter or photons from the surrounding medium. A chain of reactions then ensues:

$$
\begin{aligned}
& p + \gamma \to \Delta^+ \\
& \quad \hookrightarrow \Delta^+ \to \pi^+ + n \\
& \quad\quad \hookrightarrow \pi^+ \to \mu^+ + \nu_\mu \\
& \quad\quad\quad \hookrightarrow \mu^+ \to e^+ + \nu_e + \bar{\nu}_\mu
\end{aligned}
\qquad\qquad
\begin{aligned}
& p + \gamma \to \Delta^+ \\
& \quad \hookrightarrow \Delta^+ \to \pi^0 + p \\
& \quad\quad \hookrightarrow \pi^0 \to \gamma + \gamma
\end{aligned}
$$

The occurrence of each initial reaction depends on the surrounding matter density and the type of accelerated particle [37].

In addition to high-energy neutrinos from cosmic accelerators, EHE neutrinos are expected to be produced when UHECRs interact with the extragalactic background light (EBL) and Cosmic Microwave Background (CMB) photons via the Δ resonance (as explained in **??**). These cosmogenic, or GZK, neutrinos represent a diffuse flux and can probe the nature of the enigmatic sources of cosmic rays and the propagation of high-energy particles over cosmological distances.

Cosmogenic neutrinos contain unique information about the sources of UHECRs. The normalization and shape of the neutrino flux provide insights into the cosmic ray composition, the redshift evolution of their sources, and the maximum energy of their accelerators. Measuring the cosmogenic neutrino flux will constrain several GZK neutrino models, offering insights into the astrophysics of the highest energy particles ever detected.

EHE neutrinos present a unique opportunity to observe particles of macroscopic energies that have traveled billions of light years, revealing the maximum energy of acceleration achieved by any astrophysical source in the Universe. Furthermore, the center-of-mass energies of their interactions, approximately 10^{17} eV, surpass those of Large Hadron Collider, making them uniquely sensitive to high-energy neutrino-nucleon cross sections and exotic scenarios for physics beyond the Standard Model.

Chapter 2

Neutrino Astronomy with IceCube

Over the last forty years, one Nobel Prize per decade has been awarded for research directly related to neutrinos [1]. This underscores the importance and central role that the study of neutrinos holds in modern physics. Consequently, significant funding has been allocated, particularly for the construction of advanced detectors. The IceCube Neutrino Observatory continues this legacy by enabling groundbreaking discoveries and pushing the boundaries of theoretical physics models. Among his major contributions to astrophysics, there is the first demonstration of a flux of EHE neutrinos [7], the identification of the sources already cited in the introduction which are the blazar TXS 0506+056 [8], the nearby active galaxy NGC 1068 [9] and even the galactic plane [10], as well as the first detection of a particle shower at the Glashow resonance [38].

Although Earth is continuously bombarded by billions of neutrinos generated in the Sun and the atmosphere, neutrino detection is challenging. Experimental neutrino research relies on detecting the secondary particles produced when neutrinos interact with matter. To ensure effective detection, it is crucial to thoroughly understand these interactions and the way secondary particles are emitted in the form of a cascade.

2.1 Neutrino-matter interaction

As mentioned earlier, the key feature that makes neutrinos excellent astronomical messengers is that they can only interact with matter through the weak interaction. They interact with both nuclei and electrons. This process occurs through the exchange of a $W^{\pm}$ boson for charged current (CC) interactions or a Z^0 boson for neutral current (NC) interactions.

For energies below $100\ \mathrm{GeV}$, incident neutrinos either undergo elastic CC collisions or quasi-elastic NC collisions with hadrons. Above this energy, relevant to this work, neutrinos are directly scattered by quarks inside the hadron in a process called deep inelastic scattering (DIS). The Feynman diagrams for these interactions are depicted on Figure 2.1 with on the left NC and on the right for CC. Here each line of the nucleon N represents a quark, X is an hadronic shower and l the created lepton.

[1] 1988: Leon M. Lederman, Melvin Schwartz, and Jack Steinberger for the discovery of the muon neutrino; 1995: Frederick Reines for the discovery of the neutrino; 2002: Raymond Davis Jr. and Masatoshi Koshiba for the detection of cosmic neutrinos; 2015: Takaaki Kajita and Arthur B. McDonald for demonstrating neutrino oscillation.

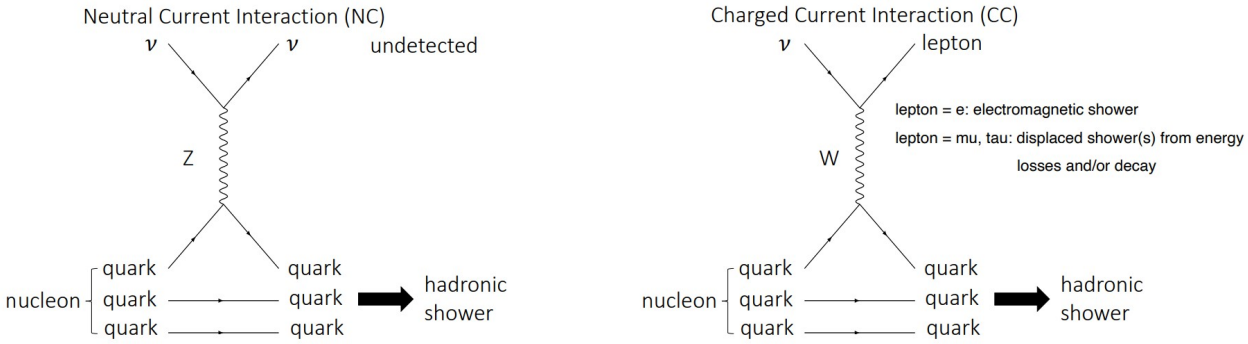

Figure 2.1: Feynman diagrams for the DIS neutral current (left) and charged current (right) neutrino interaction [42].

2.1.1 Cross-section

The cross-section of neutrinos varies greatly depending on their energy and is linked to both NC and CC interaction channels. At high energies (above $1\mathrm{GeV}$), neutrinos interact with electrons and nuclei of terrestrial atoms mainly through deep inelastic scattering processes:

$$\nu N \overset{CC}{\rightarrow} lN \qquad\qquad \nu N \overset{NC}{\rightarrow} \nu N \tag{2.1.1.1}$$

The explicit calculation of the differential cross-section for the charged current interaction with an isoscalar nucleon (i.e., with zero isospin) $N = \frac{n+p}{2}$ is given by

$$\frac{d^2\sigma^{CC}}{dxdy} = \frac{2G_F^2 M_N E_\nu}{\pi}\left(\frac{M_W^2}{Q^2+M_W^2}\right)^2 \cdot [xq(x,Q^2) + x\bar{q}(q,Q^2)(1-y)^2] \tag{2.1.1.2}$$

where M_N and M_W are respectively the mass of the target nucleon and the W boson, Q_2 the exchanged vector boson four momentum transfer which is involved in the definition of the Bjorken variable $x = Q_2/(2M_\nu)$, $y = \nu/E$ the inelasticity with $\nu = E_\nu - E_l$ the energy loss in the lab frame, G_F the Fermi coupling constant [39]. Figure 2.2 shows the evolution of the neutrino cross-section in the relevant energy range. Below 10^4 GeV, the cross-section grows linearly with the neutrino energy because the transfer momentum is much smaller than the mass of the exchange boson ($q^2 \ll M_{Z,W}$), and thus the contribution of valence quarks is dominant. At higher energies, these two quantities are of the same order of magnitude, and the contribution from the sea quarks (ud,cs) becomes dominant, causing the cross-section to enter a different regime and reducing its slope [40].

A similar reasoning can be applied to the neutral current interaction. Figure 2.2 shows the total cross-section $\sigma(E)$ combining both neutral and charged currents for neutrinos and anti-neutrinos. It varies significantly with neutrino energy as:

$$\sigma^{tot}(E) = \int dxdy \frac{d^2\sigma}{dxdy} \tag{2.1.1.3}$$

Anti-neutrinos behave in the same manner. However, due to their opposite helicity, their cross-section is approximately twice as small as that of neutrinos [25]. At energies around $1\mathrm{GeV}$, the DIS cross-

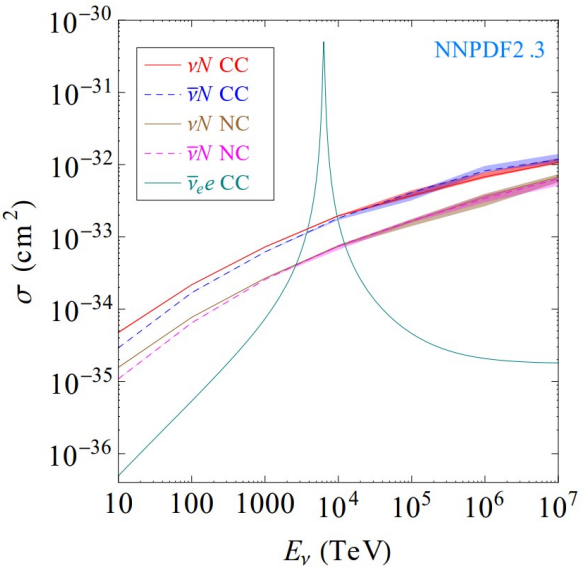

Figure 2.2: Evolution of the cross-section of neutrinos and antineutrinos as a function of their energy. The curve for $\bar{\nu}_e$ cross-section shows the Glashow resonance peak [41].

section can be approximated:

$$\sigma_{\nu p} \approx 0.69 \times 10^{-38} \left(\frac{E_\nu}{1\ \mathrm{GeV}} \right)\ \mathrm{cm}^2 \tag{2.1.1.4}$$

$$\sigma_{\bar{\nu} p} \approx 0.35 \times 10^{-38} \left(\frac{E_\nu}{1\ \mathrm{GeV}} \right)\ \mathrm{cm}^2 \tag{2.1.1.5}$$

But this difference fades when the energy goes above $\approx 10\mathrm{TeV}$. Another interesting phenomenon to mention regarding electron anti-neutrinos is the Glashow resonance effect. The Standard Model predicts the resonant formation of a W^- boson during the interaction of a high-energy electron antineutrino with an electron occurring at $E = 6.32$ PeV in the reference frame of the electron. The resonance peak is visible by plotting the evolution of the σ cross-section as a function of the antineutrino energy. This graph is presented in Figure 2.2.

In 2021, the IceCube collaboration reported the detection of a cascade of high-energy particles consistent with being created at the Glashow resonance [38]. Evidence of this phenomenon indicates the presence of electron antineutrinos in the astrophysical flux, further validating the standard model of particle physics. Moreover, its unique signature offers a method to distinguish neutrinos from antineutrinos, thereby enabling the differentiation of neutrino production processes in astronomical accelerators.

2.1.2 Penetration through the Earth

From the cross-section, it is now possible to define the interaction length, representing the mean free path of a particle before undergoing an interaction in a given medium:

$$\lambda_{int}(E_\nu) = \frac{1}{\sigma^{\nu N}(E_\nu) N_A} \tag{2.1.2.1}$$

where N_A is the Avogadro number and is expressed in cmwe (cm water equivalent) or equivalently $\mathrm{g\,cm^{-2}}$. Thus, as the cross-section increases at high energy, the interaction length decreases. Figure

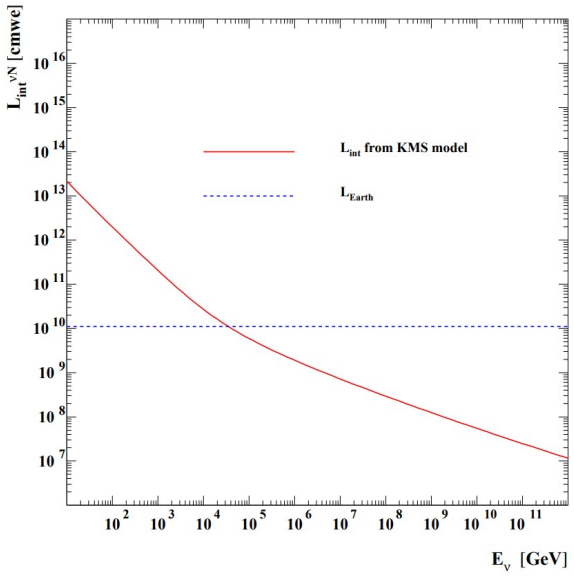

Figure 2.3: Neutrino interaction length through Earth [41].

2.3 shows the interaction length as a function of neutrino energy for a particle passing through the center of the Earth. This length is $L_{Earth} = 1.1 \times 10^{10}$ cmwe, and the energy from which the Earth begins to become opaque to neutrinos is approximately 40 TeV.

A significant attenuation of EHE neutrinos is observed around the vertical direction and decreases as the zenith angle of the incident neutrino increases. The only exception to this observation is a phenomenon called tau neutrino regeneration. This occurs when a ν_τ of energy $\gg 1$ PeV traverses the Earth. It interacts with the nucleons in the medium and creates a tau lepton, which decays extremely quickly, giving rise to another high-energy ν_τ. This process repeats many times through the Earth, and eventually, a very low-energy ν_τ emerges. Thus, even though the Earth is opaque to very high-energy ν_τ, this τ regeneration process allows for their detection [39].

2.2 Cascade Physics

When interacting with a nucleus in the detection medium, a neutrino creates a series of secondary particles. Depending on the type of this particle, this can lead to two kinds of cascades. NC interactions from all flavor neutrinos and CC interaction of numu and nutau will produce a hadronic cascade, while CC interaction of nue will additionally gives rise to an electromagnetic cascade (see Figure 2.1 for reference).

2.2.1 Electromagnetic cascade

Similar to the explanation for atmospheric electromagnetic cascades, when a high-energy electron or positron traverses a medium such as ice, it emits photons through bremsstrahlung. This phenomenon describes the radiative energy loss of a particle deflected by a magnetic field. In this case, the electron's trajectory is altered by the magnetic field of the ice atoms. The photons created in this process produce electron-positron pairs, which in turn undergo bremsstrahlung. The repetition of this phenomenon leads to an exponential increase in the number of particles and is called an electromagnetic

cascade. To approach the development of this process in a simplified manner, the Heitler model is used [25]. It considers that, at each stage of the process, an electron loses half of its energy through bremsstrahlung until its energy falls below the critical energy E_C, where losses occur through ionization rather than radiation. In this case, the maximum number of particles is given by:

$$N_{\max} = \frac{E}{E_C} \tag{2.2.1.1}$$

Thus, it depends linearly on the initial energy [43].

The integrated track length, which is the sum of all individual propagation distances (T_{em}) of charged particles in an electromagnetic cascade, scales linearly with the energy of the primary neutrino. Since the amount of emitted Cherenkov light is proportional to the track length, it also exhibits a linear dependence on the energy.

2.2.2 Hadronic cascade

The hadronic cascade occurs when the neutrino collides with a nucleon. The particles that constitute the cascade are mainly protons and neutrons, which produce charged and neutral pions. Each neutral pion then initiates an electromagnetic cascade. Thus, by approximating that at each stage of the process, a π^0, a π^+ and a π^- are created, one-third of the hadronic cascade is converted into an electromagnetic component after each step. The ratio between the track lengths due to electromagnetic part T_{em} and hadronic part T_{hadron} also represents the ratio between the quantity of Cherenkov photons produced by each of the contributions. It is given by:

$$F = \frac{T_{\mathrm{hadron}}}{T_{\mathrm{em}}} \tag{2.2.2.1}$$

This factor generally increases with energy because a larger number of π^0 are produced. The ratio is therefore rewritten in terms of the electromagnetic fraction of the cascade F_{em}:

$$F = F_{\mathrm{em}} + (1 - F_{\mathrm{em}}) \cdot f_0 \tag{2.2.2.2}$$

where f_0 is the relative Cherenkov activity of the hadronic part of the cascade. F_{em} is determined phenomenologically as:

$$F_{\mathrm{em}} = 1 - \left(\frac{E}{E_0}\right)^{-m} \tag{2.2.2.3}$$

The total length of the cascade is therefore calculable and the value found for en electromagnetic cascade is $T = T_{\mathrm{em}} = 5.21 \text{ m GeV}^{-1}$ [44]. Ultimately, electromagnetic cascades produce more Cherenkov light than their hadronic counterparts. This is due to the fact that low-energy neutrons (hence invisible) are generated in the cascade, that the creation of hadrons requires a lot of energy, thus reducing the fraction of visible energy, and that hadrons have a higher energy threshold for emitting Cherenkov photons compared to electrons [44].

2.3 The IceCube Neutrino Observatory

In November 2004, construction began in Antarctica on what would become the world's largest neutrino detector. Holes with a diameter of 60 cm were drilled to a depth of 2450 m by injecting pressurized hot water near the Amundsen-Scott South Pole Station, an American scientific base located

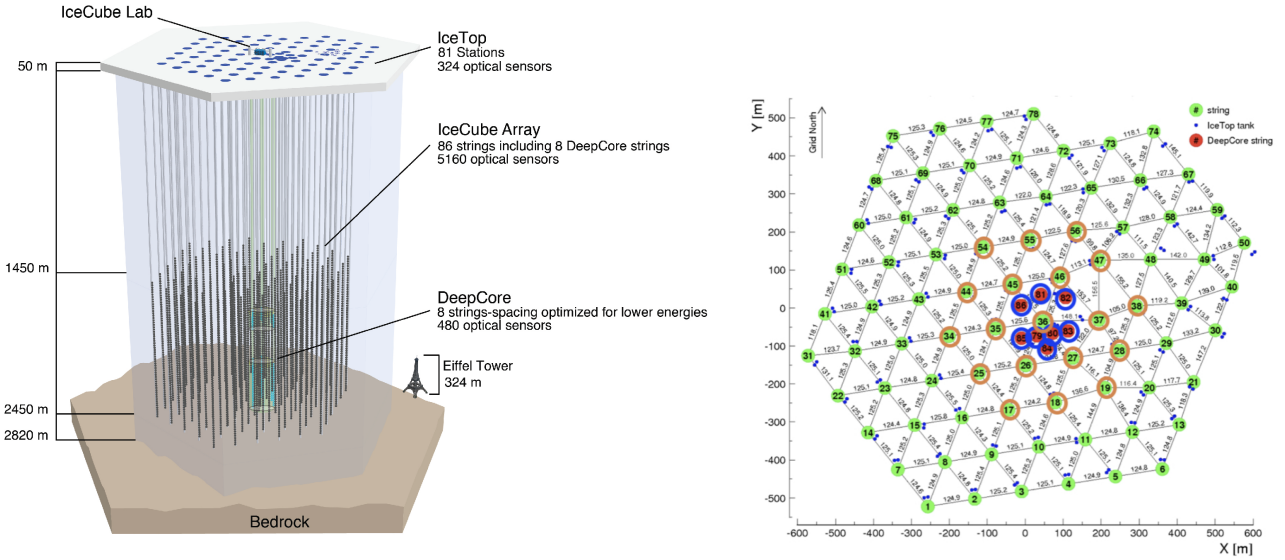

Figure 2.4: Left: Schematic representation of the IceCube Neutrino Telescope, including its"DeepCore" and the IceTop surface detector; Right: top view representation of the distribution of IceCube strings in green and DeepCore strings in red on a hexagonal grid [46].

just a few steps from the geographic South Pole. Each hole required approximately 34 hours of work followed by 12 hours for the installation of the detection modules [45]. This immense project, known as the IceCube Neutrino Observatory, is the result of an international collaboration. Its primary mission is to detect astrophysical neutrinos that had previously not been observed. Upon its completion in 2011, IceCube marked the beginning of EHE neutrino astronomy, opening a new window to the universe.

2.3.1 Detector properties

As depicted on the left-hand side of Figure 2.4, the detector consists of 5160 Digital Optical Modules (DOMs). These instruments are glass spheres with a diameter of 25 cm, housing a photomultiplier tube (PMT) on the bottom face to collect the Cherenkov light produced by charged particles resulting from neutrinos' interaction with nucleons or electrons in the ice. The bottom hemisphere is filled with silicone gel for optical coupling and contains a metal wire cage that provides protection against magnetic effects while the other hemisphere holds the entire electronic board [47]. A schematic and a picture of the DOM is shown in Figure 2.5. These optical sensors are placed on 86 strings, spaced 125 m apart, following a hexagonal grid and instrumenting a total volume of 1km^3. Each string holds 60 DOMs spaced 17 m apart. The detector has been designed to achieve the best sensitivity to neutrinos with energies ranging from 1 TeV to 1 PeV [48, 49]. An infill of the IceCube detector, called DeepCore, deploys 7 additional densely instrumented strings. DeepCore has been designed to lower the IceCube neutrino energy threshold by over an order of magnitude, to energies as low as about 10 GeV [50]. The strings and DOMs are named according to their positions on the hexagonal grid and along the string, respectively. The string numbers are shown in Figure 2.4, and the DOMs are numbered from 1 to 60 starting from the top. Each specific DOM is then identified using a coordinate pair (string, DOM).

In addition to this underground part, the IceCube Neutrino Observatory is supplemented by a

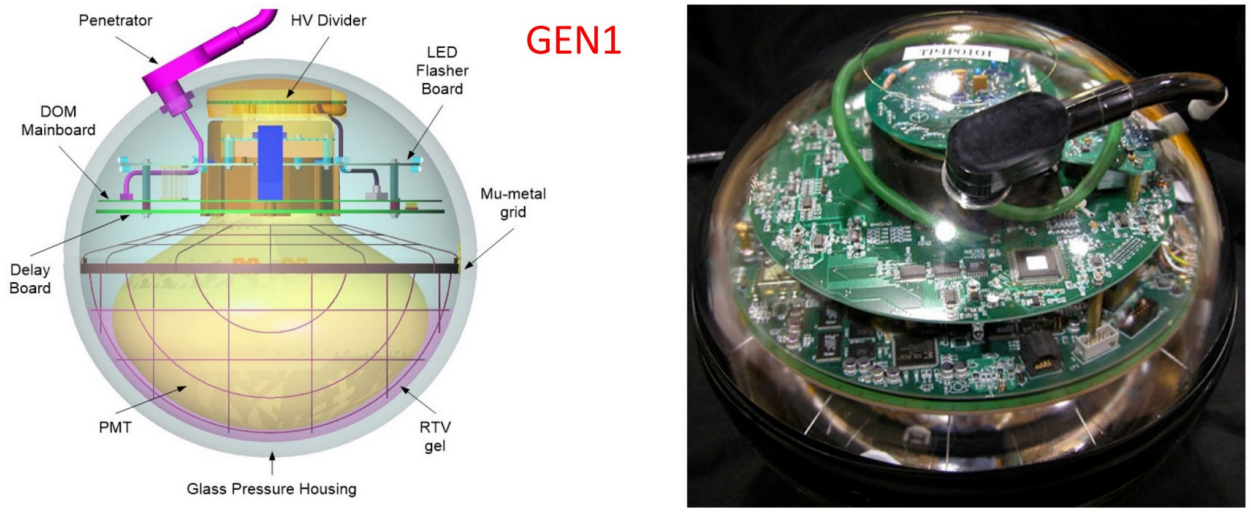

Figure 2.5: Representation on the left and photography on the right of an IceCube digital optical module (DOM) [52].

surface component called IceTop. It consists of 162 Cherenkov tanks (filled with "pure water" which froze to ice) arranged in pairs over a 1 km^2 surface at a distance of 125m from each other, above the position of each string. Each tank has two DOMs, identical to those buried in the ice. It is located at 2835 m above sea level and is built to detect atmospheric air showers of energies similar to those of the 'in-ice' detector [51]. While capable of detecting air showers and the passage of atmospheric neutrinos and muons, IceCube's primary goal is the detection of astrophysical neutrinos. Therefore, muons and neutrinos generated in the atmosphere represent a significant background.

2.3.2 IceCube coordinates

The coordinate system used in IceCube is centered at a point as close as possible to the center of the detector at a depth of 1948.07 m. It is possible to use two representations:

1. a classic right-handed Cartesian system. From its origin, the $\hat{x}$ axis is oriented along the 90-th Meridian East, the $\hat{y}$ axis along the Greenwich Meridian, and the $\hat{z}$ axis towards the surface, perpendicular to the other two. For example, the sensor closest to the origin of this reference frame is DOM (36,30) located at the position (+46m, -35m, +7m).

2. a spherical coordinate system. A common triplet (r, θ, ϕ) is then employed. The angle θ is the zenith, defined as the angle between the vertical $\hat{z}$ and the line connecting the particle to the origin, and ϕ is the azimuthal angle, described as the projection of this same line in the $x - y$ plane measured counterclockwise from the +x axis. In this reference frame, the northern sky is defined as the part of the celestial sphere with $\theta > 90\,\mathrm{deg}$, i.e., the northern hemisphere seen from the South Pole. This reference frame is used to refer to the direction of the particle passing through the detector.

Thus, most of the time, a particle is located within the detector using the five coordinates (x, y, z, θ, ϕ), the first three giving its position and the last two characterizing its direction [53].

2.3.3 Detection Principle

The neutrino-matter interaction creates a hadronic and possibly electromagnetic cascade of relativistic secondary particles, which can be detected through the Cherenkov light they produce in the ice.

Cherenkov radiation

In 1934, during his thesis, Pavel Alekseyevich Cherenkov observed a faint emission of continuous spectrum in a volume of transparent liquid. He explained the reasons for this in an article four years later [54] and was awarded the Nobel Prize for this discovery in 1958. In this paper, he explained that when a charged particle traverses a dielectric medium at a speed greater than that of light in this same medium, some of its energy is transferred to the surrounding polar molecules. These molecules, attracted by the charge, align themselves as the particle passes through. Upon returning to their initial state, they emit light. Thus, if the charged particle has a speed greater than that of light, this collective effect of the medium's molecules results in a coherent conical electromagnetic emission, known as Cherenkov radiation [55].

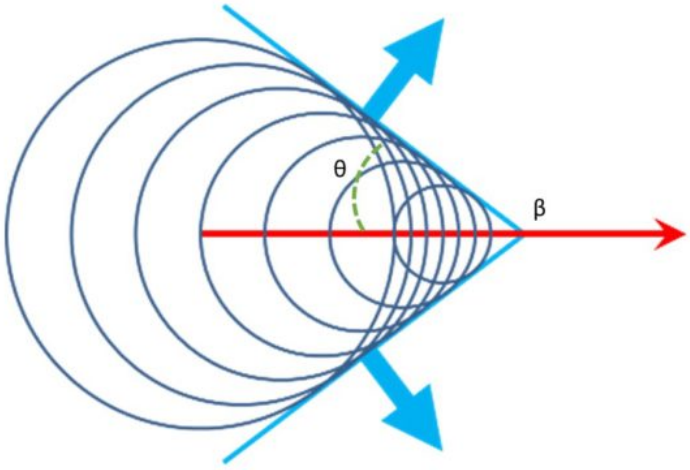

Figure 2.6: Illustration of emission of Cherekov radiation [56].

The threshold for production of Cherenkov radiation is given by:

$$v_{part} = \beta \cdot c > c_{med} = \frac{c}{n} \Rightarrow \beta > \frac{1}{n} \tag{2.3.3.1}$$

where c and c_{med} are respectively the speed of light in vacuum and in the medium, v_{part} the particle speed, β the Lorentz factor and n the refractive index of the medium.

IceCube utilizes the extremely transparent ice of the Antarctica as its (natural) detection medium. The properties of this ice have been studied in detail, and the average refractive index of deep ice is established to be close to $n \approx 1.78$ at IceCube's depth[2] [57]. Thus, the particle emits light at a characteristic angle called the Cherenkov angle, which is obtained via the following relation:

$$\cos\theta_C = \frac{c/n}{\beta \cdot c} = \frac{1}{\beta n} \tag{2.3.3.2}$$

[2]Obviously, these values are not constant throughout the detector and must be adjusted at each point of the detector. For more information, the reader is referred to [58].

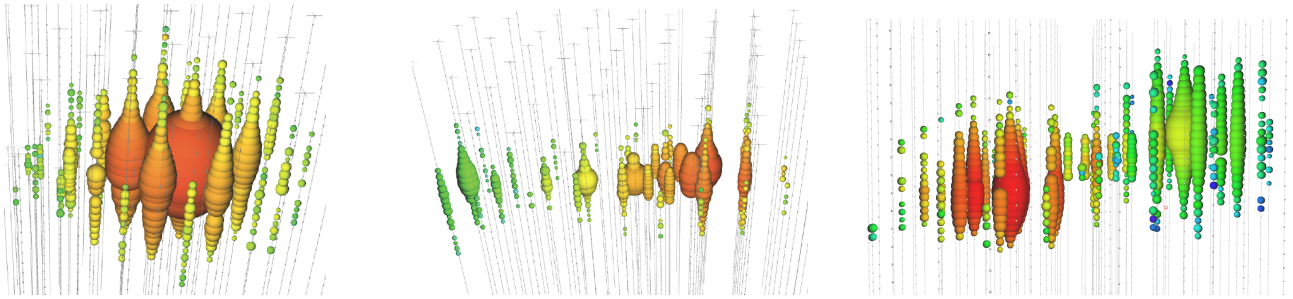

Figure 2.7: From left to right, cascade signature, track signature and double bang signature. The color indicates the arrival time, with red representing earlier detection times and green representing later detection times. The size of the colored spheres represents the amount of photons collected by the DOM [59].

For a relativistic particle ($\beta \approx 1$) and assuming a constant index of refraction ($n = 1.78$), the Cherenkov angle has a value of $\theta_C \approx 56°$ [58].

Signatures and detection rate

IceCube uses the total charge collected by the DOMs and the photons arrival time to infer neutrino properties such as energy and direction. Depending on the primary neutrino interaction type, three different in-ice signatures can be detected [60, 61]:

- *Cascades:* They originate from an electromagnetic or hadronic shower resulting from a CC interaction of ν_e or ν_τ and NC interaction of neutrinos of all flavors. The secondary particles composing the cascade move radially from the vertex. Furthermore, due to the spacing of the DOMs and the scattering of photons during their journey through the ice, these cascades possess an almost spherical light distribution, clearly visible in the left part of Figure 2.7.

- *Tracks:* They are created by a CC interaction of ν_μ. The central illustration of Figure 2.7 shows an example of the track generated by the produced muon. This track-like shape is formed by the Cherenkov light emitted by the muon as well as the hadronic cascade that appears at one of its ends. Above TeV energies, these tracks have typical lengths on the order of kilometers, which is too large to be fully contained within the detector.

- *Double bang:* It occurs during the CC interaction of a ν_τ following $\nu_\tau + N \to \tau + X$. This interaction generates a visible hadronic cascade in the detector. The τ has a lifetime of 29 ps during which it propagates. However, when E_{ν_τ} is in the PeV range, it does not have enough time to exit the detector (it travels roughly 50m) before decaying via: $\tau^- \to \mu^+ + \bar{\nu}_\mu + \nu_\tau$ (BR $\approx 18\%$), $\tau^- \to e^- + \bar{\nu}_e + \nu_\tau$ (BR $\approx 18\%$) or $\tau^- \to \nu_\tau +$ meson (BR $\approx 64\%$) This gives rise to a second cascade also visible in IceCube. An example of this event is shown in Figure 2.7.

It is possible to approximate the neutrino detection rate of the IceCube detector. Since the first two types of events described above are predominant in the detector, it is acceptable to estimate this rate by calculating the flux of muon tracks and cascades appearing in the detector [25]:

$$R(E_{\text{vis}}, \theta) = \int_{E_{\text{vis}}} P_{\nu \to \ell}(E_\nu, E_{\text{vis}}) P_{\text{shadow}}(\theta, E_\nu) \frac{dN_\nu}{dE_\nu} dE_\nu \tag{2.3.3.3}$$

This formula encompasses three fundamental components:

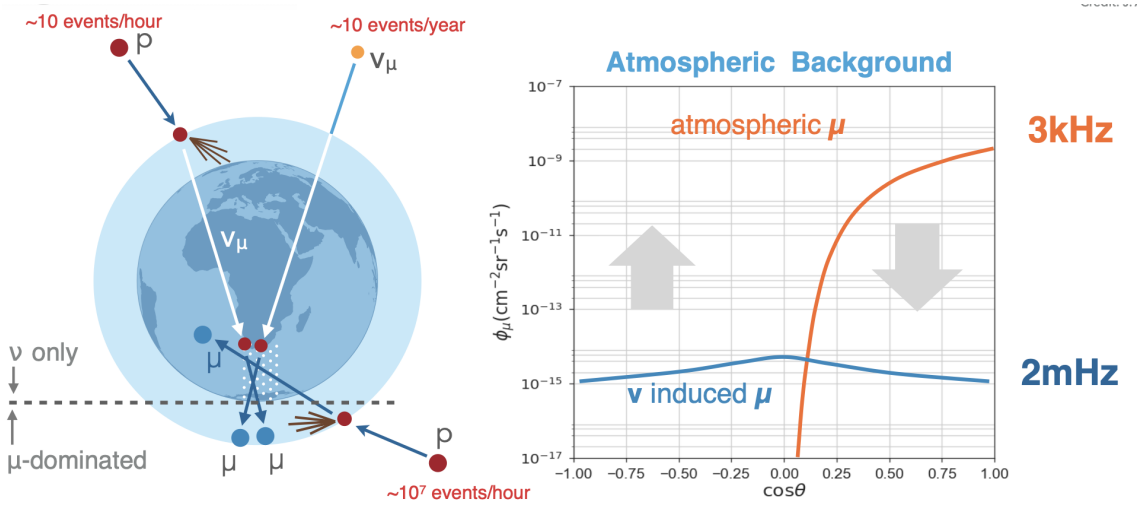

Figure 2.8: Atmospheric background in IceCube, including muons and neutrinos from cosmic-ray-induced air showers (left) and Atmospheric background flux (right). Credit: J.A. Aguilar.

- The likelihood of a neutrino generating a detectable event within the detector, either by producing a lepton or a particle cascade. The probability is expressed as:

$$P_{\nu \to l} = N_A \int_{E_{min}}^{E_\nu} dE_l \frac{d\sigma}{dE_l} r_l(E_l, E_{vis}) \tag{2.3.3.4}$$

  where r_l denotes the detection range necessary for generating the lepton (μ) or the EM or hadronic cascade with an energy of E_l. The event must attain a final energy of E_{vis} in order to generate a detectable amount of light, and $\frac{d\sigma}{dE_l}$ represents the neutrino interaction cross-section.

- The attenuation of the neutrino flux as it traverses the Earth. Consequently, P_{shadow} signifies the probability that a neutrino, arriving at a zenith angle θ with energy E_ν, is absorbed by the Earth. By defining $\xi(\theta)$ as the column depth of Earth traversed by the neutrino with a zenith angle θ, and recalling that the mean free path of the neutrino is delineated by equation 2.1.2.1, the attenuation of the Earth is computed as:

$$P_{shadow} = e^{-N_A \sigma_{tot} X(\theta)} \tag{2.3.3.5}$$

- The incident neutrino flux at surface, denoted as $\frac{dN_\nu}{dE_\nu}$.

Atmospheric background

Thanks to its large volume and high sensitivity, IceCube collects an impressive amount of data at a rate of approximately 3 kHz.

Figure 2.8 shows the atmospheric background in IceCube, including muons and neutrinos from cosmic-ray-induced air showers, cf. section 1.1.1. Atmospheric muons represent the most significant contribution in the Southern Sky (downward-facing region), while they can be filtered out by looking at the Northern Hemisphere, as they cannot traverse the Earth. However, atmospheric neutrinos represent an irreducible background (with a rate of mHz) for astrophysical searches, since they can traverse the Earth and cannot be removed using the Earth as a filter. It is often only possible on a

statistical level to differentiate between astrophysical and atmospheric neutrinos because an event-by-event classification is impossible. In this situation, the neutrino energy spectrum is often used to improve the distinction.

For the contribution coming from the South, an outer layer of DOMs is considered a veto zone for neutrino interaction vertices (see Figure 2.9). Thus, only events occurring inside the detector are retained, i.e., those for which the DOMs veto layer don't receive any light [61].

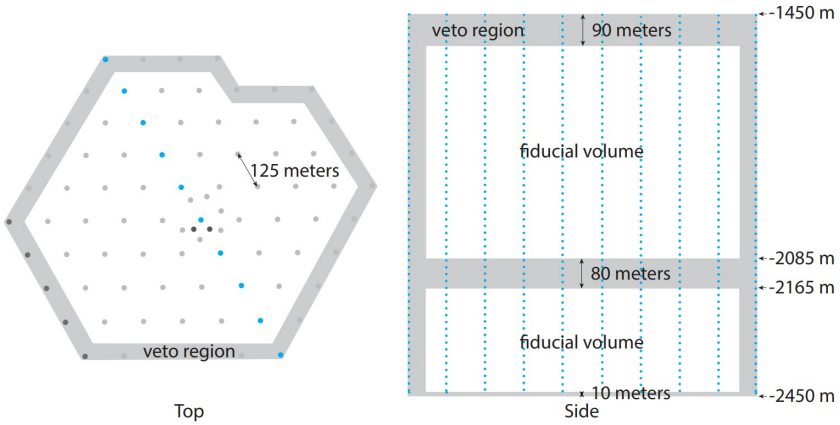

Figure 2.9: Veto Zone in IceCube: aerial view (left) and sectional view (right) [61].

As explained previously, the use of the earth as a filter has an impact on the detection of neutrinos with energies greater than $1\ \mathrm{PeV}$. Indeed, as their cross section increases, they interact by crossing the Earth, only allowing their detection close to the horizon in the Northern hemisphere.

Data format

All the data collected (or simulated) is stored in *.i3* files. The objective of this format is to compress a large amount of information into minimal memory space. The data is meticulously organized within *.i3* files, consisting of a series of frames containing precise information. These frames can vary in nature depending on their content: Physics (P), Data Acquisition (Q), Detector Status (D), Calibration (C), Geometry (G), Tray Info (T) and Simulation (S). The Q type is arguably the most crucial as it contains event information along with detector readings, whereas other types of frames typically contain information about the detector, ice, etc., such as G frames. Different event data is distributed within these frames in the form of I3Table, identified by a key, representing the types of data contained therein. Another noteworthy frame type is the P frame, which exclusively contains event-related information derived from the Q frames through a separation process [62].

While the initial format is adept at storing and transferring data, it's less ideal for analysis purposes. Hence, *.i3* files are often converted into *.hdf5* format, where only a subset of the data (chosen by the analyzer) is retained. Similar to *.i3* files, data in *.hdf5* format is organized into groups within which named datasets are stored [63].

2.3.4 Reconstruction methods for cascade events

Finally, these data are analyzed, and the main characteristics of the event are determined through its reconstruction. The IceCube collaboration has developed several different reconstruction techniques

for different event signatures and energies. They have in common that they typically rely on using a predictive model to fit an event hypothesis to the measured data using a likelihood model.

A common example is a technique that uses a cascade template composed of numerous spline tables generated for cascades of various vertex positions and directions of incidence via Monte Carlo simulation explained in detail in the 3.2.2 section. It utilizes a log-likelihood method to determine which simulation best matches the recorded data to infer the properties of the event [64].

For instance, the total energy deposited by a cascade can be determined by comparing the number of photons measured at every DOM with the predicted one via spline tables. Since photon detection follows a Poisson distribution, the probability of detecting k photons when the average number of detected photons is λ, is given by:

$$P(k;\lambda) = \mathcal{L} = \frac{\lambda^k}{k!} e^{-\lambda} \tag{2.3.4.1}$$

Since the spline tables are generated with a constant energy E_0, the prediction for a cascade with an arbitrary energy E is obtained by linearly scaling the mean predicted number of photons with the energy $\lambda' = E/E_0\lambda$. Equation 2.3.4.1 thus becomes energy-dependent:

$$\mathcal{L} = \frac{(E\lambda)^k}{k!} e^{-E\lambda} \tag{2.3.4.2}$$

The following equality can be established directly:

$$\ln \mathcal{L} = k \ln(E\lambda) - E\lambda - \ln(k!) \tag{2.3.4.3}$$

It is then possible to maximize the likelihood with respect to energy by considering the detection made by each DOM:

$$0 = \left.\frac{\partial \Sigma \ln \mathcal{L}}{\partial E}\right|_{E=E_{\max}} = \sum_{\text{DOMs}j} \left(\frac{k_j \lambda_j}{E\lambda_j} - \lambda_j\right) = \sum \frac{k_j}{E_{\max}} - \sum \lambda_j \tag{2.3.4.4}$$

The most probable energy $E_{\max}$ that results in detecting k photons is given by:

$$E = \sum k_j / \sum \lambda_j \tag{2.3.4.5}$$

These calculations are generalized by adding a term ρ representing the number of photons generated by the detector noise. Thus, the mean is given by $\lambda = \lambda E + \rho$ and Equation 2.3.4.3 becomes:

$$\ln \mathcal{L} = k \ln(E\lambda + \rho) - (E\lambda + \rho) - \ln(k!) \tag{2.3.4.6}$$

The maximization is then expressed as:

$$0 = \sum \left(\frac{k_j \lambda_j}{E\lambda_j + \rho_j} - \lambda_j\right) \tag{2.3.4.7}$$

The energy that maximizes the likelihood of detecting k photons is obtained by applying gradient-descent numerical minimization algorithms to the following equation:

$$\sum \lambda_j = \sum \frac{k_j \lambda_j}{E\lambda_j + \rho_j} \tag{2.3.4.8}$$

It is possible to include a time dependence by evaluating the probability not per DOM, but per time interval. However, this only slightly improves the energy reconstruction but is crucial for direction reconstruction [65].

Chapter 3

Simulation in IceCube

The IceCube detector is designed to capture Cherenkov photons emitted by ultra-relativistic particles created during the interaction between a neutrino and an ice nucleus. It records the temporal distribution and flux of photons captured by the DOMs.

The goal of a simulation is to replicate these data as accurately as possible. To achieve this, the used algorithms must be capable of recreating the following elements in sequence:

1. the neutrino-nucleon interaction,
2. the creation and propagation of secondary particles,
3. the emission and propagation of Cherenkov photons emitted by these particles,
4. the detector response,
5. the simulation of electronic noise and background from air showers.

Each of these steps has been implemented (in C++ or Python) and can be used within the IceCube's core software framework IceTray, a comprehensive suite designed to establish a cohesive analysis environment, accommodating simulation, reconstruction, and analysis modules seamlessly. This framework encompasses various integral components, including Dataclasses for efficient data storage, the event viewer, Input/Output file utilities, and versatile tools facilitating interaction with external services like databases [66].

3.1 Simulation Steps and Software

The simulation process is intricate and multifaceted, requiring a diverse set of software tools tailored to different stages. Furthermore, the steps involved in producing the final signal exhibit diverse formats. Figure 3.1 describes the simulation steps and Figure 3.3 shows the data types contained within the I3Frames, produced at each stage of the event simulation and reconstruction in IceCube.

3.1.1 Primary Particles, Vertex, and Secondary Particles

IceCube detects different type of events as described in section 2.3.3. Given the significant differences among these particles, it is impractical to simulate them all in a single process. Hence, various software packages have been used, each specializing in a particular simulation domain.

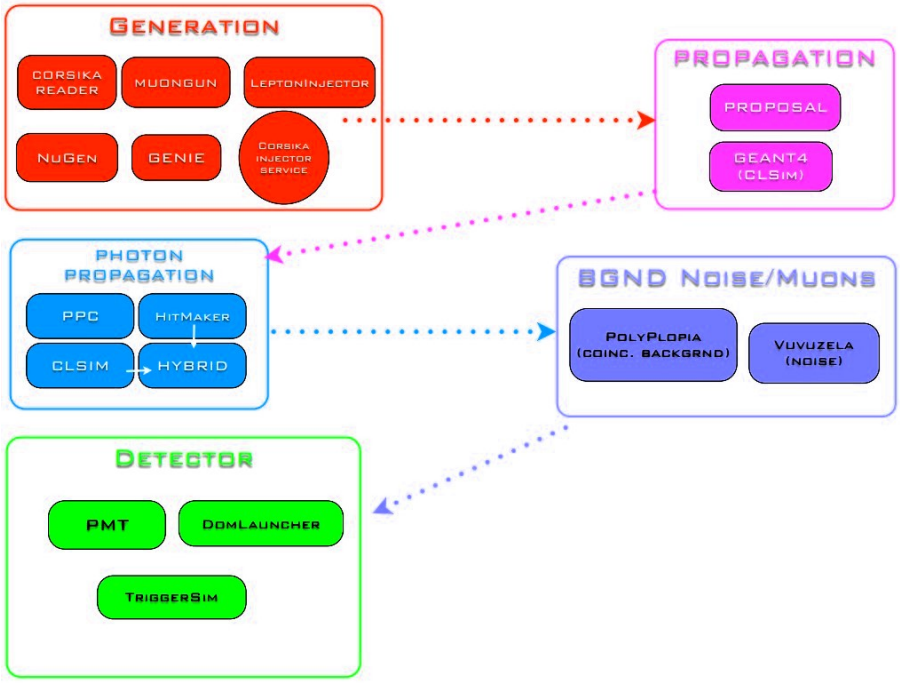

Figure 3.1: Software tools used for successive stages of simulation in IceCube [67].

- The CORSIKA software, short for COsmic Ray SImulation for KAscade, is utilized to replicate the cosmic-ray air showers detected by IceTop. Employing a Monte Carlo technique, CORSIKA accurately models the trajectories of primary particles, such as protons, photons, nuclei up to iron, or other particles, through the atmosphere until their decay or interaction with an air molecule. In the second case, the software also simulates the Extensive Air Showers initiated along the propagation direction. This framework can effectively simulate events ranging from 10^{12} to 10^{20} eV in energy [68].

- As mentioned earlier, atmospheric muons are abundantly produced in the atmosphere, penetrating the ice surface and reaching the detector. For these events, a Monte Carlo generator known as MuonGun is employed. This tool, based on CORSIKA simulations, parametrizes the flux of atmospheric muons reaching the detector's depth, allowing for the simulation of only those muons contributing to the detection process, thereby optimizing computational efficiency [69].

- Various codes are available for simulating neutrinos and their interactions in the ice. Among these, NuGen (Neutrino Generator) and LeptonInjector are the most commonly used. NuGen synthesizes a neutrino of a particular flavor and determines its energy and direction of incidence (θ, ϕ), the zenith and azimuthal angles. It injects the particle or its antiparticle with a $(1 : 1)$ ratio at at a certain distance from the surface of Antarctica (depending on the particle's energy). Subsequently, the software propagates the neutrino through the Earth and makes it interact if necessary. The code takes into account both charged and neutral interactions with Earth's nuclei, as well as the Glashow resonance and tau regeneration, both explained in section 2.1. Secondary particles are then absorbed by the Earth, and the simulation stops unless a second neutrino is created, in which case it continues its path.

  If the neutrino reaches the detector, NuGen, using an occurence probability, simulates a vertex within the detection volume. The NC and CC interactions are both considered. NuGen also

manages the situation in which multiple neutrinos would arrive simultaneously at the detector except the situation where two neutrinos interact simultaneously. The probability of the latter case occurring is so low that if it were to happen, NuGen would choose one of only two neutrinos to interact. Finally, secondary particles, including electromagnetic and hadronic cascades resulting from them, are created with their own direction and energy [70].

LeptonInjector operates on the same principle as NuGen, except that the interaction weighting part is included in an additional component of the software called LeptonWeighter. Like NuGen, its generation is Monte Carlo-based [71].

- The PROPOSAL (Propagator with Optimal Precision and Optimized Speed for All Leptons) is a Monte Carlo-based software used to simulate muon and tau propagation through a transparent medium. This software pays special attention to the numerous physical phenomena associated with this propagation, such as ionization, bremsstrahlung, photonuclear interactions, electron pair production, etc., as well as the treatment of uncertainties in the simulations [72].

The simulation volume is therefore different from the effective detection volume, as the simulation begins outside the detector and can continue after passing through it, as in the case of muons. The primary and secondary particles created during these simulations are stored in a Q frame, inside an object called *I3MCTree*. They take the form of *I3Particle*, which is a class that manages to describe them and their kinematics, recording some parameters. Among these, there are at least position (3 coordinates), time, direction (2 angles), energy, length, and speed [73]. Afterwards, they are propagated in the ice using the PROPOSAL and CMC (Cascade Monte Carlo) software to account for interactions with the medium such as ionization, electron-positron pair production, bremsstrahlung, photonuclear interaction, and decay.

3.1.2 Cherenkov emission and light propagation

The data collected by the DOMs are the number of photons detected and their temporal distribution. The aim of this simulation step is to accurately predict these parameters and, consequently, the probability density function (PDF) of the arrival time of photons.

To achieve this, the Cherenkov emission by secondary particles and the propagation of each photon through the ice must be simulated. This step requires significant computational power because the number of photons can be very high and their paths very complex.

The most accurate method relies on numerical ray tracing of each individual photon using a Monte-Carlo (MC) simulation. Softwares like clsim [74] or PPC [75] for Photon Propagation Code allows for this simulation but it demands computational power that increases rapidly with the event's energy. This is why another technique, called Photonics, was developed and has been widely used. This method uses results from the previous approach and approximations to reduce the amount of computation required.

In the same vein, more recently, new event reconstruction techniques based on deep learning have been developed. The convolutional neural network Event-Generator is one of them. Giving the success in event reconstruction of this method in particular, it is therefore interesting to adapt this tool for event simulation, as it could address both the computational power issue and reduce the number of approximations made. Since this work aims to evaluate the reliability of this method's predictions by comparing it to the other two, these techniques are discussed extensively in sections 3.2 (MC & Photonics) and 3.3 (Event-Generator).

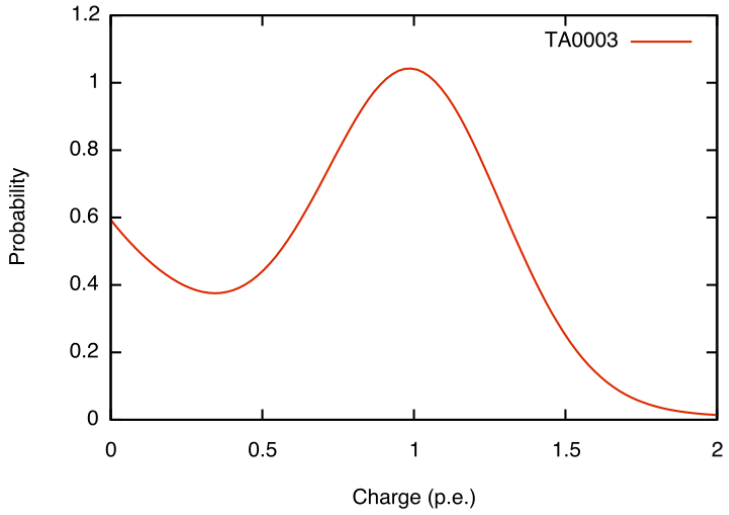

Figure 3.2: Charge response function probability distribution model used to weight the MCPEs to account for the variability in photoelectron amplification by the PMT [76].

3.1.3 Detector Response

The aforementioned methods simulate the light yield at each DOM in the from of Monte Carlo Photoelectrons, abbreviated as *MCPEs*. To obtain a replica of the signals as collected by the detector, it is essential to simulate the noise that occurs during detection, as well as the response of the photomultipliers (PMT) and the DOM.

- The noise that appears between the production and the recording of photons consists of three distinct parts: uncorrelated radioactive noise, uncorrelated thermal noise, and correlated noise, all of which generate detectable photons. The first is due to the electronic properties of the PMTs and the DOMs, which are temperature-dependent. It is simulated by a Poisson distribution:

$$f_{\text{Uncorrelated}}(x) = \frac{(\lambda\Delta t)^x}{x!} e^{(-\lambda\Delta t)} \tag{3.1.3.1}$$

  where Δt is the simulated time window and λ is the parameter describing the rate of photons hitting the detector, called *hits*, of the described process. A similar Poisson process to equation 3.1.3.1, but independent of temperature, describes the number of hits generated by the decays occurring in the glass of the DOMs and the PMTs. Finally, the correlated noise arises from secondary particles due to the previous decays. These produce a burst of photons through scintillation. This large number of photons hitting the detector simultaneously is followed by a long afterglow. The hits from this part are given by a Poisson distribution independent of the time window:

$$f_{\text{Correlated}}(y) = \frac{\eta^y}{y!} e^{-\eta} \tag{3.1.3.2}$$

  where η is an experimental parameter approximately equal to 8. Their time interval follows a standard normal distribution:

$$f_{\text{Correlated}}(z_i) = \frac{1}{\sqrt{2\pi}} e^{-z_i^2} \tag{3.1.3.3}$$

  where z_i results from the time δt_i between two successive hits via a log-normal distribution:

$$\delta t_i = 10^{(\mu+\sigma z_i)} \tag{3.1.3.4}$$

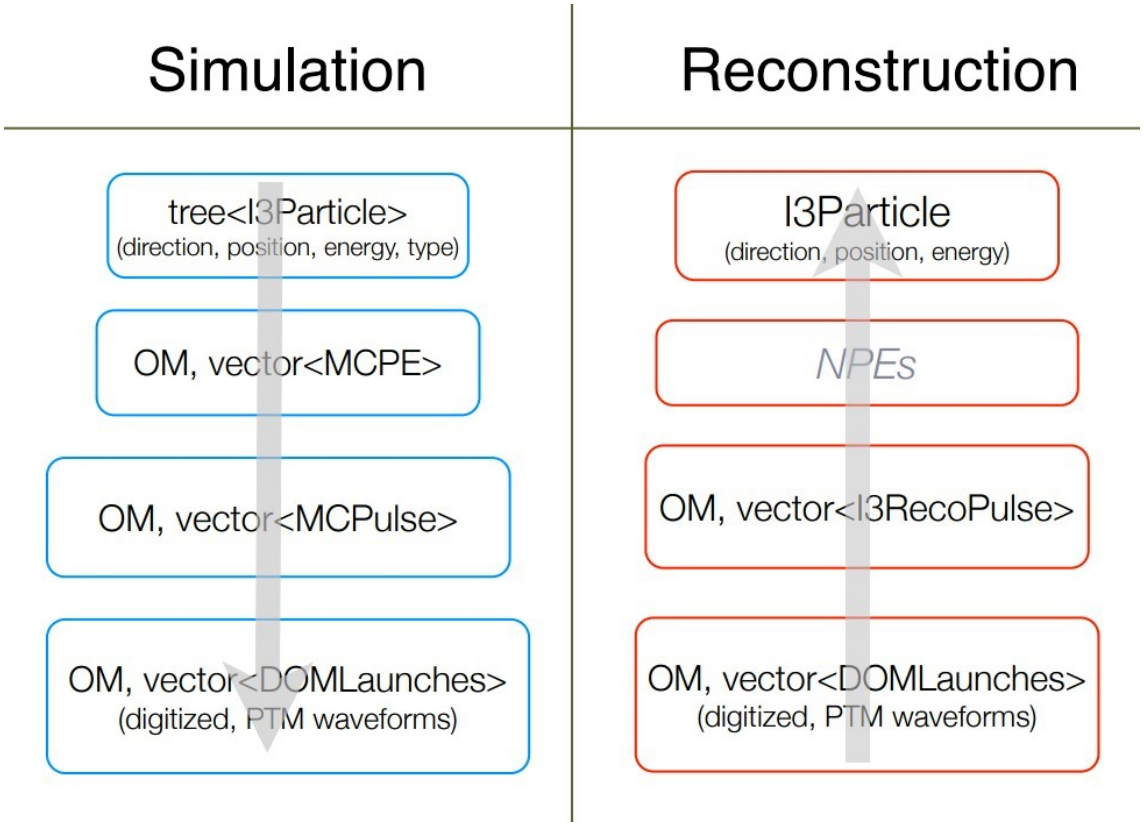

Figure 3.3: Types of data produced at each stage of event simulation and reconstruction in IceCube [67].

These three components are simulated by the software Vuvuzela, which produces modified MCPEs data [77].

- PMTResponseSimulator takes the MCPEs created in the previous steps as input and calculates the charge deposited on the anode at each hit. A weight corresponding to the charge carried by the photon is assigned to each MCPE using a charge response function probability distribution model. This model, shown in Figure 3.2, combines a Gaussian centered on a charge of 1 photoelectron and an exponential to account for low-amplitude signals. This assignment is essential as it simulates the variability in signal amplification by the PMT.

  Next, the software simulates the pre-pulses, late pulses, and after-pulses[1], the variable transit time of the photoelectrons in the PMT, the temporal resolution of the hits of 2 ns, and saturation effects. The outputs are of the type *MCPulses* [67].

- The DOMLauncher code concludes this simulation sequence by replicating the behavior of the DOM mainboard. This consists of a discriminator that imposes a temporal threshold and an amplitude threshold for the detected signal for each DOM, local coincidence logic that ensures the signal has been detected by several neighboring DOMs, and signal digitization. The input signal is thus an MCPulse, while the output signal is a *DOMLaunch* [78].

[1]Pre-pulses are formed by electrons ejected from the first dynode, late pulses by electrons backscattered from the dynode and hitting the cathode, and after-pulses result from ionizations of residual gas between the dynodes caused by the passage of accelerated electrons.

The different types of data obtained at each stage of the simulation are shown on the Figure 3.3. In this case, the collected signal is obviously a DOMLaunch. To reconstruct the event properties it is desirable to first estimate the number of photons hitting the DOM by removing the detector response again. In this case, the obtained signal is in the form of an *I3RecoPulse*. An Ice Tray segment named DetectorSegment can be used to obtain I3RecoPulses data by taking MCPEs or MCPulses as input [67].

3.2 Full Monte-Carlo simulations and Photonic method

The crucial aspect of simulating an event in Icecube is the determination of the number of photons and their temporal distribution detected by each DOMs. A method, referred to here as full Monte Carlo simulation, allows for the precise simulation of each photon's propagation in the ice from their point of emission to where they are detected. However, the number of photons to be simulated (especially in UHE events) and the non-trivial optical properties of the ice, make this step particularly challenging. As this method requires significant computational power and takes a considerable amount of time, the photon distributions calculated are stored in large tables called spline tables.

Another method, Photonics, which has been widely used in recent years, was then implemented. It interpolates these tables to obtain the probability distribution function associated with each DOM for a given event hypothesis, i.e., a particle cascade. Despite some approximations involved, Photonics must deliver an accurate simulation while minimizing computational time and power, and store the data in the most accessible and concise manner possible [12].

3.2.1 Light propagation and Ice properties

Before discussing the full Monte Carlo simulation itself, it is important to examine the propagation of Cherenkov photons through the ice. It is influenced by absorption and diffusion processes. With the Cherenkov effect in ice emitting photons in the visible or near UV spectrum, absorption is primarily due to molecular and electronic excitations. The absorption length λ_a is defined as the average distance after which a Cherenkov photon is absorbed. Polar ice is also embedded with air bubbles (near to the DOM) and dust grains, which act as scattering centers. Given their varied sizes, the most appropriate theory to explain their influence on photons is Mie scattering. For each scattering event, characterized by the size of its scattering center and the wavelength of the photon, this method predicts a scattering angle distribution.

The optical properties of the ice significantly influence photon propagation. Therefore, it is crucial to accurately model the characteristics of the cubic kilometer of ice in which the detector is submerged. Antarctic ice has accumulated over millennia and thus exhibits variations in its optical parameters with depth. Indeed, differing conditions of pressure, temperature, and insoluble dust have resulted in successive layers that can be approximated as horizontal, this greatly facilitates their simulation.

3.2.2 Monte Carlo Simulation and spline table

The objective of this part of the simulation is to obtain the arrival time and flux of photons emitted by a stationary point-like source for each DOM. This is achieved using the full Monte Carlo method. The source is characterized by an orientation and position, and the light emitted has an emission angle and wavelength from the Cherenkov emission profile.

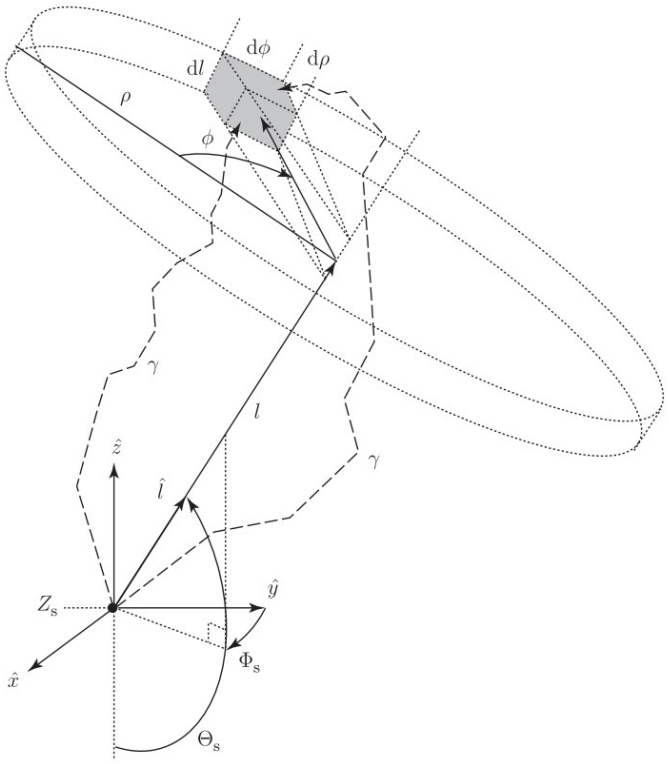

Figure 3.4: Propagation of photons emitted by a source located at position Z_s, and the geometry of the recording cells used to determine the photon flux [12].

The coordinate system chosen to describe the propagation and recording of photons is cylindrical (ρ, l, ϕ). This preference arises from the cylindrical symmetry exhibited by the Cherenkov cone in a non-dispersive medium. Despite the disruption of this symmetry by the optical properties of the medium, the coordinate system remains intact. Additionally, the system is aligned, by design, with the symmetry axis of the source, denoted as $\hat{l}$, as shown in Figure 3.4.

The path of the photons is then simulated from scattering point to scattering point, and a weight characterizing their probability of reaching the next point without being absorbed is updated at each scattering, considering the properties of the surrounding ice. The position of the photon in this reference frame is recorded each time it enters a recording cell, a volume element representing a potential recording point. The system's symmetries are exploited to reduce the number of parameters to save. Only the recording position relative to the source, the source depth Z_s along the vertical axis $\hat{z}$, the zenith angle Θ_s, and the recording time t are placed in a six-dimensional table called the spline table. It contains a series of bins whose width is the time between two recordings. Each of these bins contains the differential flux of photons arriving in a cell, weighted by the total weight of the detected photons. Each source with a particular position or orientation will generate its own spline table. By repeatedly simulating the same source a large number of times, the PDF of photons reaching a chosen detection point and the expected flux are obtained. A parameterization of these functions is then stored in the spline tables, increasing their size.

3.2.3 Photonics method: spline tables interpolation

When simulating events with Photonics, it is no longer necessary to numerically calculate the propagation of photons. It is sufficient to load the spline tables, produced by the previous technique, corresponding to the studied source. In the case of a moving source, its trajectory is approximated as a series of closely spaced point sources. This is done using the PhotonicsService package available in the IceTray environment. The mean field of photons reaching a DOM is then calculated for each DOM and the total field produced by a source of specific energy is recorded. If the DOM is not adequately placed on a fictitious detection cell for a single source, or if it receives light from multiple point sources, a multidimensional interpolation of the spline tables is performed to calculate the PDF of photons reaching the DOM.

3.3 Event generator method

Since 2013, the fully installed IceCube Neutrino Observatory has been recording as many events as possible to detect and study astrophysical neutrinos. Since particles of this type are rare, finding them requires deeper analysis of this gigantic quantity of data. It is for this reason that ever more efficient and more economical methods of reconstruction and simulation have been developed. In this idea, the IceCube collaboration has turned towards a method that requires very low computational power, once the code is trained, and is very powerful: neural networks.

Various types of neural networks have been developed over the years, initially for reconstructing events. Among them, convolutional neural networks (CNNs) have stood out due to their excellent adaptation to the data provided by the detector and their exceptional ability to exploit the system's symmetries. It is this type of neural network that a new event reconstruction method called EventGenerator [11] uses. Designed to exploit the symmetries and domain knowledge studied, this method is coupled with a usual model of maximum-likelihood based technique to obtain the best possible outcomes. It shows good results for the reconstruction of high energy cascade events [11] and it has been crucial in the discovery of EHE neutrinos from the galactic plane [10]. This success suggests the potential use of this neural network for simulating EHE events, with the major advantages of saving computational resources compared to full MC and reducing approximations in comparison with Photonics.

This subsection first provides the theoretical considerations of this type of neural network. Finally, an explanation of the main components of the NN are presented. Given the complexity of the process, the explanation is limited to the reconstruction and simulation of cascade events, although these models could be applied to other signatures.

3.3.1 Neural Network and Training: theoretical considerations

Neural Network Description

As its name suggests, a neural network consists of a large number of small computational units called neurons. These neurons are arranged in successive layers, referred to as the input layer for the first, the output layer for the last, and hidden layers for all those in between. These artificial neurons are connected to each other in various ways, thereby defining different types of neural networks. For instance, left part of Figure 3.5 depicts a fully connected network where each neuron in a layer is connected to all neurons in the previous and consecutive layer.

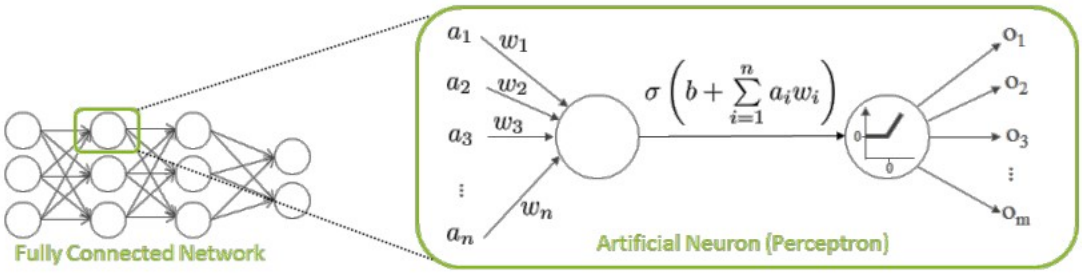

Figure 3.5: Fully connected neural network and zoom on the calculations carried out inside a neuron [79].

A neuron in a layer thus receives data a_i from the neurons in the previous layer. Within each neuron, a specific weight is assigned to each input before a weighted sum is computed. A bias term b_i is then added to this sum. These parameters, $w_i j$ and b_i, are optimized during training. The result is subsequently processed through a nonlinear activation function $\sigma(x)$. The most common activation functions are shown in Figure 3.6. Their purpose is to enable the neural network to process nonlinear relationships in the data [79].

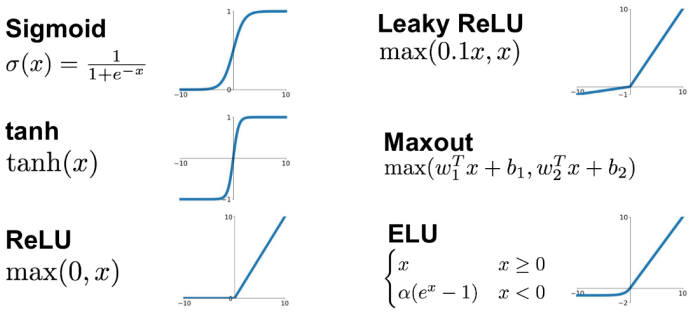

Figure 3.6: Main activation functions used in neural networks [80].

Convolutional Neural network

The IceCube collaboration is developing different types of NN whose characteristics are adapted to its detector. Among them are convolutional neural networks (CNN). Initially developed for image recognition, CNNs take advantage of the fact that relationships between pixels at the top of an image are not causally related to those between pixels at the bottom. Consequently, it is not necessary to consider connections between them. Moreover, when an object is moved from one location to another inside the image, its nature and thus the pattern attributed to it by the CNN remains unchanged. In other words, convolutional layers leverage locality and translational invariance to eliminate some unnecessary free parameters.

Convolutional layers have the capability to share weights associated with the input data of one neuron to another. This weight sharing forms what is known as a convolutional kernel or filter. Using the analogy of image processing again, this means that a feature detected in one part of the image can be applied to another part of the image. Figure 3.7 illustrates the calculation of a convolutional layer (horizontal green surfaces) composed of 25 neurons. To achieve this, a kernel of size 3×3 consisting of 9 units moves laterally across the blue input layer to produce the green output layer. To obtain an output, the kernel weights the shaded part of the input layer before summing their contributions. The

collection of these outputs forms the feature map. Naturally, if the kernel size changes, the feature map also changes. A convolutional layer can also have multiple kernels [79].

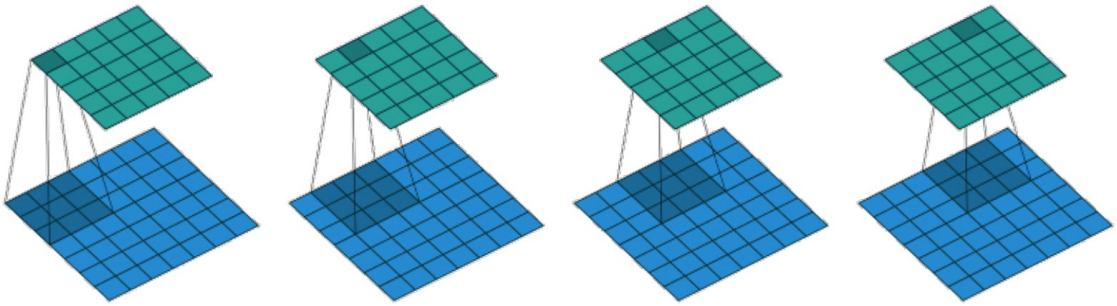

Figure 3.7: Convolutional kernel of 9 units moving laterally across the blue input layer to produce the green output layer [79].

These features echo the temporal and spatial translation invariance of neutrino physics described in subsection 2.1. However, while image pixels are small and easily arranged in an orthogonal grid, CNNs are designed to process this specific arrangement in input data. This poses a challenge because IceCube's data has large and variable dimensions, and originate from DOMs distributed on an irregular triangular grid. This is discussed in detail in section 3.3.2.

Training Procedure

The training of a neural network is carried out in three stages. First, it is essential to determine a loss function that best characterizes the disagreement in the networks outcome with the true value. The goal of the training process is to minimize this function.

It is also necessary to create a specific dataset where the input data is associated with the actual value that the neural network needs to determine. For example, using the analogy of image recognition, the training set will contain data in which an image of an y_{true} is already associated with the class y_{true} that the neural network must identify.

The dataset is then divided into n "batches". The second step involves passing these data through the neural network, which then returns an output $f_\theta(x)$. The loss function $L(f_\theta(x), y_{\text{true}})$ thus characterizes the errors the neural network makes by comparing its output with the expected true response y_{true}. This process is illustrated on the left side of Figure 3.8.

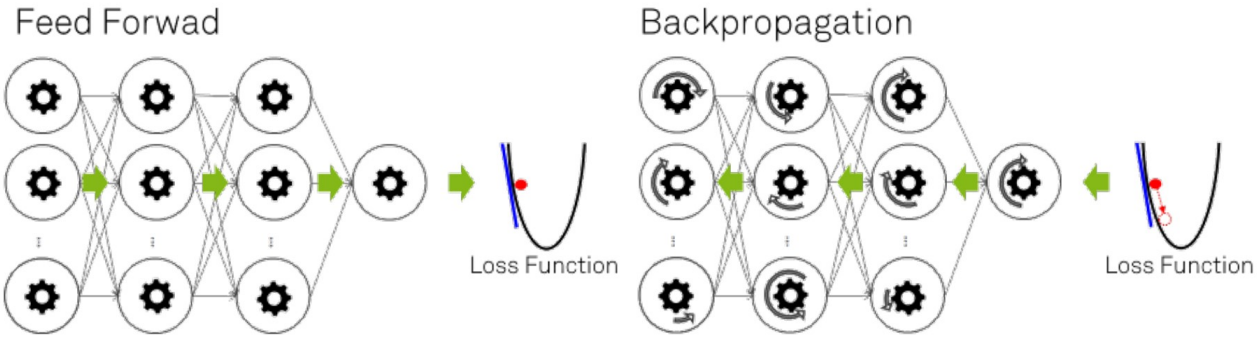

Figure 3.8: Illustration of determining the loss function through forward propagation and calculating the gradient via backpropagation [79].

The initial outputs of the neural network will be random values because the free parameters θ of the neural network are initialized this way. The final step minimizes the loss function to adjust these parameters. To achieve this, stochastic gradient descent is employed. For each batch, backpropagation calculates the gradient $\frac{\partial L}{\partial \theta}$ with respect to the free parameters. This step is shown in Figure 3.9. This process is iteratively repeated until the losses converge to a minimum [79, 82].

The initial dataset used during the training process is divided into three parts: the training set, the validation set, and the test set. Only the first set is used during the previously described stages. The second set is used to determine if the parameters resulting from the training process are performing correctly. If the process has been carried out properly, the curves describing the evolution of losses as the training progresses for both the training and validation sets will tend similarly towards a small value. Normal training is illustrated in the central part of Figure 3.9. If at some point, the losses evaluated on the validation dataset start to increase, creating a gap between the two curves, this behavior is called overfitting. This situation is shown in the right part of Figure 3.9. Overfitting can occur, for example, due to excessive memorization of the training data, and applying this to another set creates a divergence. In that case, the training is then stopped at the point where the validation losses are minimal. The last set is used by the NN to evaluate the entirety of the training and not for further training. The difference from the validation set is that no parameters are determined when it is presented to the NN [81].

Another process used to improve training and reduce the likelihood of overfitting is the dropout. This technique involves randomly removing units from certain layers of the NN to reduce the likelihood of the training process placing too much emphasis on specific data.

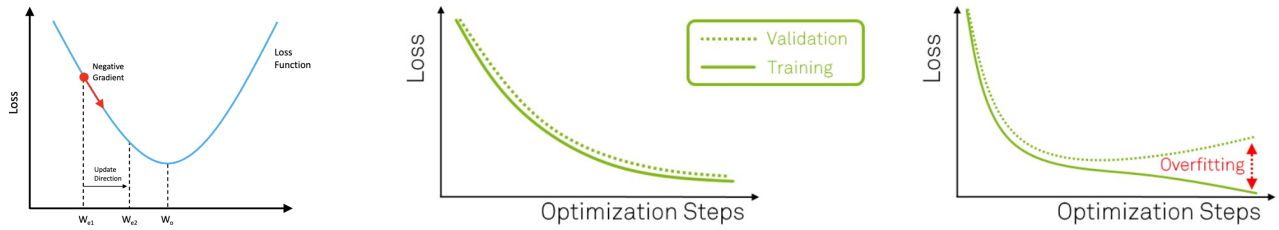

Figure 3.9: In the graph on the left, a representation of gradient descent aimed at reducing losses is shown [82]. Representations of the loss evolution evaluated on the training set and the validation set during training are presented in the central and right parts, respectively, illustrating the cases where the training proceeds correctly and in the case of overfitting [79].

3.3.2 IceCube Features and Implemented Software

IceCube's Hexagonal Geometry and Data Dimensionality

Most convolutional algorithms rely on data storage and tensor operations based on an orthogonal grid. This means that IceCube's data must be converted to this format, despite the detector being composed of three parts with an approximately hexagonal shape but different sizes: the main section has 78 string of 60 DOM spaced 17 m apart, the upper DeepCore (related to the dust layer) has 10 DOMs spaced 10 m apart on 8 strings and the lower DeepCore has 50 DOMs spaced 7 m apart on 8 strings too.

Each of these parts is treated independently to achieve an orthogonal framework. For the DeepCore section, this is accomplished by unfolding the hexagon into a two-dimensional line: the number

of strings in length and the number of DOMs in height. For the main part, fictitious zero DOMs are added to form a cube with a face of (10×10) strings and a depth of 60 DOMs. The modification of the detector geometry is shown in Figure 3.10, where the added zero points are indicated in orange.

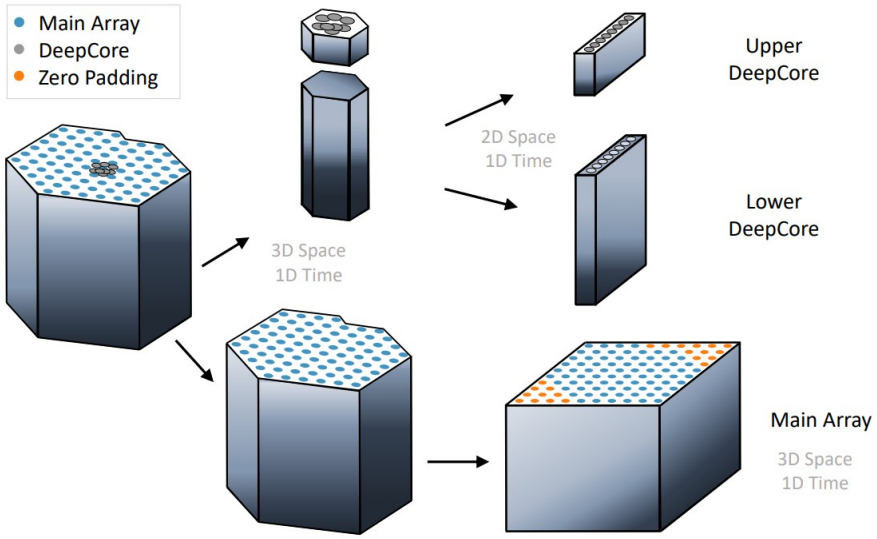

Figure 3.10: Orthogonalization process of the three hexagonal-shaped detector parts of different size [65].

However, it is important to note that this transformation does not accurately approximate highly irregular areas of the detector, such as the dust layer. The modification of the input grid results in the following input data tensors: $(10 \times 10 \times 60 \times n)$ for the main part, $(8 \times 10 \times n)$ for the upper DeepCore, and $(8 \times 50 \times n)$ for the lower DeepCore. In these tensors, n is the number of parameters describing the cascade event and the DOMs. Generally, CNNs require input data to be of uniform and constant shape, which means that n cannot vary [65].

Hexagonal Convolution Kernels

To determine the kernel shape that best fits the input geometry, the same method as in the previous subsection is employed. The original hexagonal arrangement is placed on a parallelogram-shaped grid, which is filled with zeros at its edges. It then appears that using a hexagonal-shaped kernel makes it possible to preserve the geometry of the detector. It is defined by a size s and orientation o, encapsulated in a tuple (s, o). Figure 3.11 shows different hexagonal kernels, defined by various tuples. It also illustrates the completion of the grid with zeros, represented by orange points [65].

Preprocessing: Data Normalization

In principle, the range and scaling of a data set should not be an issue for neural networks, able of handling a vast amount of data. However, most nonlinear activation functions used in these neurons are centered around zero. This means that if they are applied to very large or very small data, they converge and the associated gradient vanishes. Additionally, a dispersion of data over several orders of magnitude creates an asymmetry in the distribution of errors. As a result, the gradient no longer consistently points toward the minimum, causing issues during training. An illustration of this problem is shown in Figure 3.12, where an asymmetric elliptical error distribution presents a gradient vector that does not point toward the minimum, unlike the circular distribution where it does.

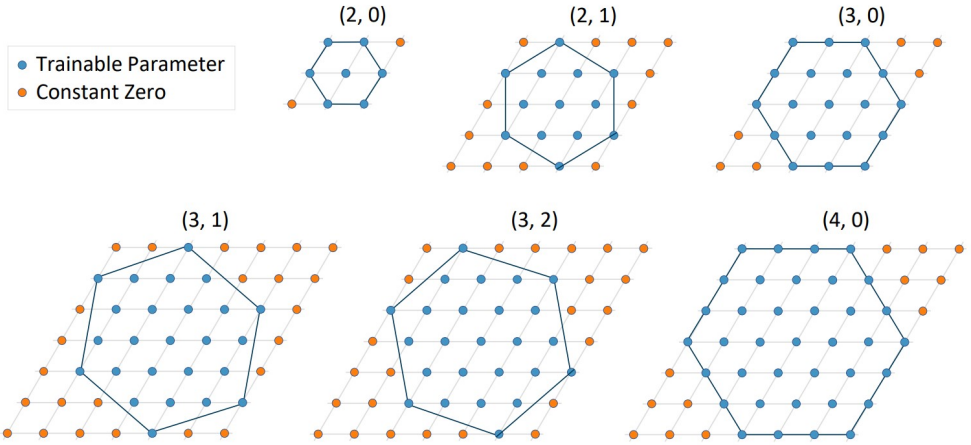

Figure 3.11: Hexagonal convolutional kernel defined by a tuple (s, o) where the size s corresponds to the number of points on one edge of a kernel with orientation $o = 0$ [65].

Some data collected in IceCube (such as energy or collected charge) span several orders of magnitude and thus lead to these kinds of problems. These values undergo the following transformation:

$$X' = \ln\left(C + X\right) \tag{3.3.2.1}$$

where the constant C ensures that the logarithm does not receive a null value. Other data remain unchanged: $X' = X$.

Another problem related to input data that can occur is the exploding gradient. This effect happens when a small imbalance due to non-normalized data propagates through the NN, causing an excessive increase in the gradient during backpropagation. To prevent this, the input data are normalized to zero mean and unit variance via:

$$X'' = \frac{X' - \overline{X'}}{\sigma_{X'} + \epsilon} \tag{3.3.2.2}$$

where $\overline{X'}$ is the mean and $\sigma_{X'}$ is the standard deviation derived from a subset all events prior to the training. The constant $\epsilon = 10^{-4}$ is included to avoid division by zero. Finally, this data transformation ensures that the X' and $\sigma_{X'}$ from the elements added to fill the grid, in orange in Figure 3.10, are zero. Thus, their output in X'' also remains zero.

Figure 3.12: Representation of the error distribution and the associated gradient vector for an asymmetric elliptical distribution on the left and a circular distribution on the right [79].

3.3.3 Event-generator method: Combining Maximum-Likelihood and Deep Learning

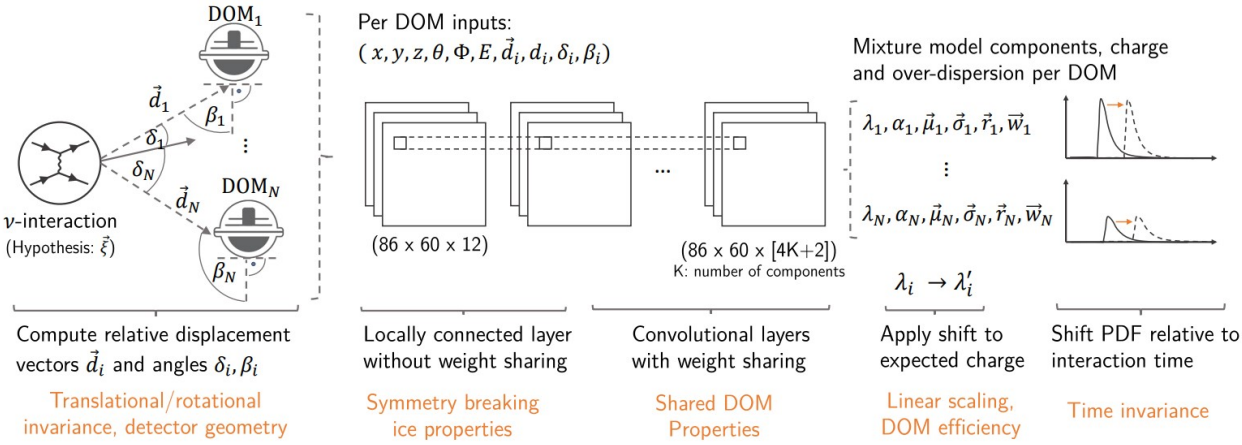

Figure 3.13: Event-Generator method architecture [11].

In contrast to Photonics, employing a neural network allows to involve more dimensions for the prediction of the photon yield at each DOM. This increased complexity should allow, considering a successful training of the network, for a more accurate prediction. The use of neural networks is therefore emphasized since they allow for efficient interpolation of large amounts of data and, once trained, require very little computational power. Event-Generator in addition to having the advantages of deep learning, is coupled with a maximum-likelihood setting to achieve the best possible performance.

The first step is to implement a cascade event generative neural network which, for a given cascade hypothesis, returns the charge $\vec{\lambda}$ and the pulse arrival time PDF $\vec{P}(t)$ reaching a DOM. This generative model simulating a cascade which is described by the following parameters: $\vec{\xi} = (x, y, z, \theta, \Phi, E, t)$ is denoted:

$$G(\vec{\xi}) = \{\vec{\lambda}, \vec{P}(t)\} \tag{3.3.3.1}$$

The function that best models the pulse arrival time PDF $P_d(t)$ for a particular DOM d is a mixture of asymmetric Gaussians. These are defined by:

$$AG(x|\mu, \sigma, r) = N \cdot \begin{cases} \exp\left(-\frac{(x-\mu)^2}{2\sigma^2}\right), & x \leq \mu \\ \exp\left(-\frac{(x-\mu)^2}{2(\sigma r)^2}\right), & \text{otherwise} \end{cases} \tag{3.3.3.2}$$

where r is the parameter describing their asymmetry and N is given by:

$$N = \frac{2}{\sqrt{2\pi} \cdot \sigma(r+1)} \tag{3.3.3.3}$$

The pulse arrival time PDF is a weighted sum of K Gaussians:

$$P_d(t) = \sum_{j=1}^{K} w_j \cdot AG(t|\mu_{(d,j)}, \sigma_{(d,j)}, r_{(d,j)}) \tag{3.3.3.4}$$

This method has the advantages of requiring only a small value of K (between $K = 3$ and $K = 5$ suffices) to obtain a good description and of maintaining a low number of free parameters.

In order to reduce approximations from the start, the exact position of each DOM relative to the center of the cascade (primary interaction point) is calculated and this relative displacement vector provided as input to the network. In addition to this data, the different angles shown on the left part of the Figure 3.13 are determined and feed to the network. This allows both rotational and translational symmetries to be preserved along with the detector geometry.

These pieces of information, combined with those of the cascade, form a tensor of size $(86 \times 60 \times 12)$ containing all the DOMs, which is sent as input data to a CNN where the data weights are not shared among the DOMs because the kernel is of dimension 1×1. This neural network serves to simulate the symmetry breaking that occurs in the ice. The data is then sent to a second layer of the CNN but with shared weights to simulate other properties such as the quantum efficiency ϵ_d of the DOMs or the linear scaling of the collected charge. This is done by modifying the expected charge through the relation:

$$\lambda'_d = \lambda_d \cdot \frac{E}{10\text{TeV}} \cdot \epsilon_d \tag{3.3.3.5}$$

The overall architecture of the method is presented in Figure 3.13. The outputs it returns are therefore $\vec{\mu}_d, \vec{\sigma}_d, \vec{r}_d, \vec{w}_d$, the parameters of the mixture model, and the charge λ_d collected by each DOM. It is also important to add that the charge is scaled based on the energy at the end of the process.

Although it is designed for event reconstruction, the neural network employed as constructed can be used for generating or simulating events.

During the training, a Gamma-Poisson mixture distribution is apply on the pulses measured at the DOMs. It is given by:

$$\text{GammaPoisson}(z \mid \lambda, \alpha) = \frac{\Gamma\left(z + \frac{1}{\alpha}\right)}{\Gamma(z+1)\Gamma\left(\frac{1}{\alpha}\right)} \left(\frac{1}{1+\alpha\lambda}\right)^{\frac{1}{\alpha}} \left(\frac{\alpha\lambda}{1+\alpha\lambda}\right)^{z}, \tag{3.3.3.6}$$

It is simply an equivalent of the usual negative binomial distribution but real-valued. The α that appears in Equation 3.3.3.6 is the shape parameter that characterizes the dispersion of the photons. The likelihood of obtaining an event given N_d pulses at the d-th DOM, each one arriving at time $t_{d,i}$ and carrying a charge $c_{d,i}$, is [11]:

$$\mathcal{L}_{\text{event}}\left(\vec{x} = \{\vec{c}, \vec{t}\} \mid \vec{\xi}\right) = \prod_{d=1}^{5160} \text{GammaPoisson}\left(\sum_{i=1}^{N_d} c_{d,i} \mid \lambda_d(\vec{\xi}), \alpha_d(\vec{\xi})\right) \cdot \prod_{i=1}^{N_d} P_d(t_{d,i} \mid \vec{\xi})^{c_{d,i}}. \tag{3.3.3.7}$$

Chapter 4

Evaluation of the Event-Generator Simulation

The Event-Generator model, initially developed for event reconstruction, is now adapted to make simulations in IceCube. To assess its reliability, its predictions are first compared to those obtained using the photonics method, cf. section 3.2, for EHE incident neutrinos. Then, MC simulation will be added to the analysis for incident neutrinos of 10 TeV. This work focuses only on event cascades and the analysis is conducted by studying one of their main characteristics: the total collected charge predicted for each DOM or over the entire event.

4.1 Cascade event simulation

The first step is to simulate a cascade and visualize the PDFs created by each method. A cascade is defined by: $\xi = \{(x, y, z), \theta, \phi, E, t\}$ where (x, y, z) are the vertex coordinates expressed in the IceCube reference system, θ, ϕ and E are the zenith angle, azimuth angle, and energy of the incident neutrino, respectively, and t is the time at which the interaction occurs. When this cascade is injected into the detector, a PDF is predicted for each DOM using Photonics and Event-Generator methods separately. Figure 4.1 is a graph showing a comparison of the PDF generated at DOM $(36, 30)$ by each of these techniques for a $E = 10$ TeV cascade generated at the center of the detector, i.e. at position $(0\text{ m}, 0\text{ m}, 0\text{ m})$. This sensor is closest to the vertex. Its location is recorded at $(+46\text{ m}, -35\text{ m}, +7\text{ m})$. It should be noted that while Event-Generator predicts the temporal distribution of reconstructed photon pulses, Photonics predicts the hits of MC photonelectrons.

It logically follows that the farther the DOM is from the interaction point, the wider their temporal dispersion and the larger the time at which the distribution is centered. The first behavior arises from the fact that the photons are differently scattered during their journey, spreading out their arrival time and extending their travel time before being detected. This evolution is evident when the PDFs from a cascade are plotted for all the DOMs in a string for one interaction point. Figure 4.2 shows the PDFs for DOMs 4 to 50 of string 36.

As previously, the closest point to the vertex in this case is DOM 30. On the graphs, the PDFs are very similar for DOMs close to the cascade center but differ increasingly with greater distance. Ultimately, a significant difference appears in both the PDF and the predicted charge for the farthest DOMs represented. Photonics seems to predict a distribution where this is not the case for

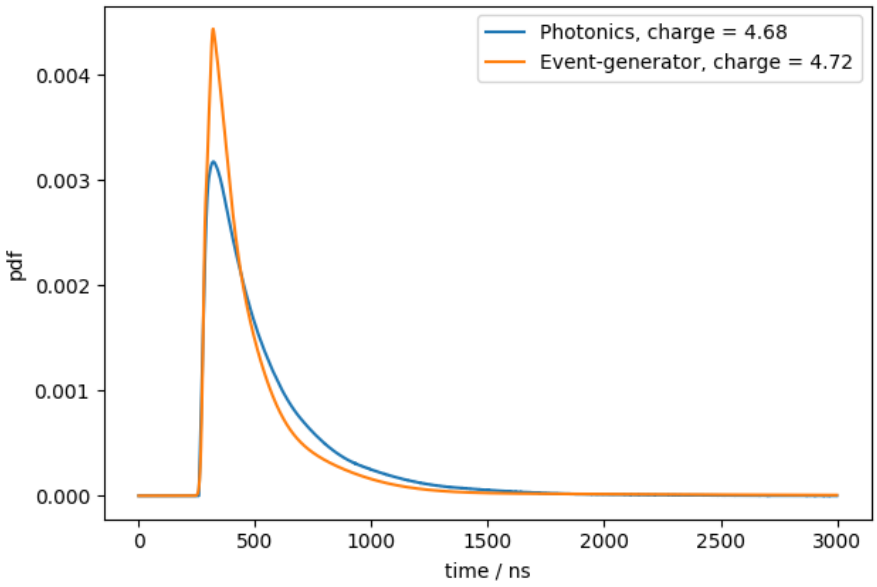

Figure 4.1: Normalized PDF generated at DOM $(36, 30)$ *by the photonics method (blue) and the Event-generator method (orange) for a* 10 TeV *cascade with vertex at (0,0,0). The mean expected charge is indicated in the legend.*

Event-Generator. This is attributed to a larger background for Photonics than for Event-Generator, the second being invisible due to share scales. Physically, the PMTs are too far from the center of the cascade to record a signal from the cascade.

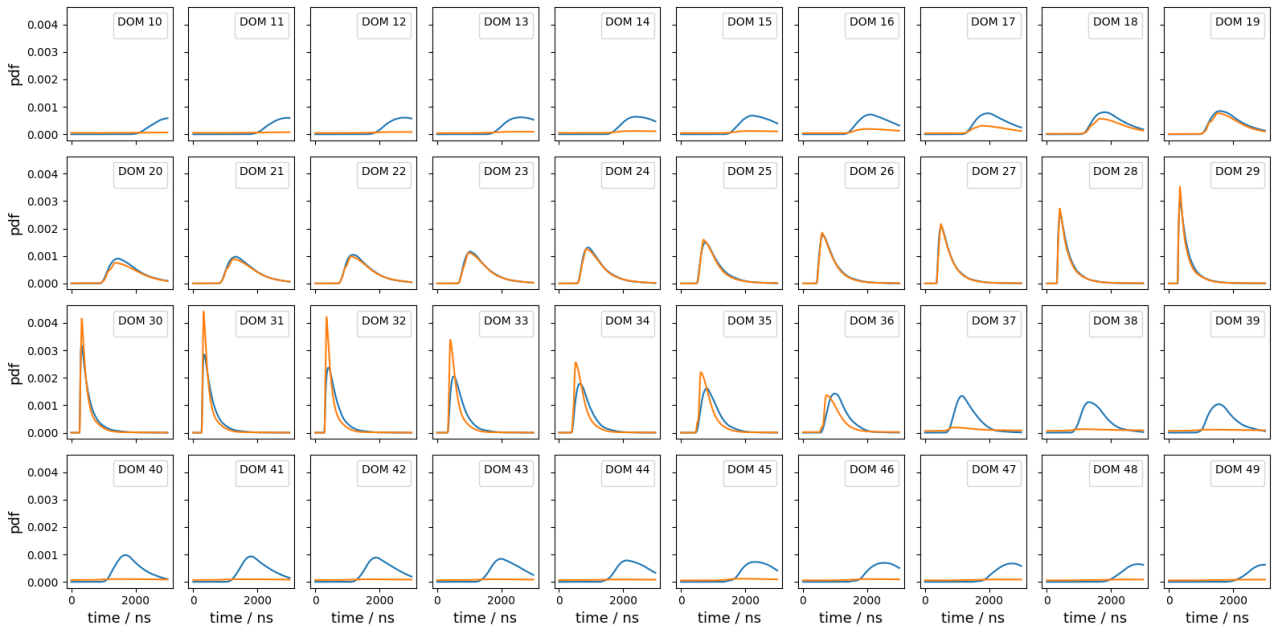

Figure 4.2: Normalized PDF generated by the Photonics method (blue) and the Event-generator method (orange) at DOMs 4 to 50 of string 36 for a 10TeV *cascade with vertex at* $(0, 0, 0)$.

It is also possible to predict the charge received by each DOM. This value is indicated in the legend of Figure 4.1. Generally, this charge is expressed in units of photoelectrons. The value is obtained by dividing the collected charge by the charge of an electron multiplied by the nominal gain of the PMT [83]. In these simulations the charge of each photoelectron is normalized to 1 by dividing this number by the incident charge. The way the charge collected by a sensor is predicted differs between methods:

- Photonics uses a Poisson distribution for the description of photoelectrons in each DOM giving the predicted mean charge λ.
- Event-Generator uses a negative binomial distribution for the description of photoelectrons in each DOM. This time, the distribution is defined properly by the mean number of photoelentrons and the binomial coefficient α.

The total charge collected by each DOM for the same event is shown in Figure 4.3. This time a detector simulation has been performed based on the prediction of Photonics and for each DOM actual photon hits have been sampled for both methods (e.g., in each DOM the actual simulated charge can vary from the predicted mean following the aforementioned probability density distributions). Each colored point represents a DOM that receives a charge. They are distributed according to their distance from the vertex in the $x - y$ plane and their position on the string on the vertical axis. This allows consideration of the 3D geometry of the detector in a 2D representation. Only detection points close to the vertex exhibit significant charge, which decreases spherically with distance, consistent with the interpretation derived from the PDFs. An asymmetry is observed between the propagation upwards in the detector and downwards. This is due to the presence of the dust layer, which increases absorption and scattering in the ice. Consequently, the light yield within and below this layer is significantly reduced.

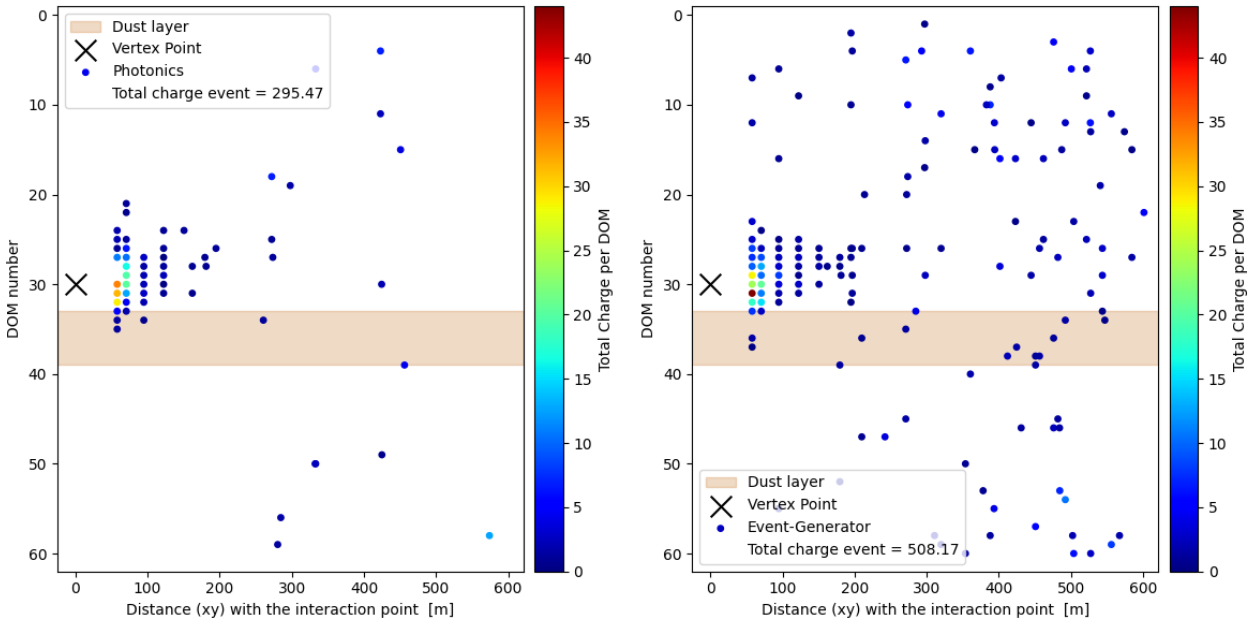

Figure 4.3: Total charge collected by each DOM for a 10 TeV cascade with a vertex at (0,0,0) with Photonics on the left and Event-Generator on the right.

The presented comparison so far was established for an incident neutrino energy of $10\ \mathrm{TeV}$, which is relatively low. By increasing the energy, some adjustments are useful to make. Three phenomena are interesting to mention to obtain an adequate simulation at high energy.

1. A cascade event in IceCube consists of both a hadronic and an electromagnetic part. As described previously, at low energies, the electromagnetic component produces more Cherenkov photons than the hadronic component. The latter is therefore simulated as an electromagnetic cascade but at a lower energy. This difference decreases with increasing energy, resulting in the hadronic component's contribution becoming more significant and approaching that of the electromagnetic component.

2. The sources of Cherenkov photons, which are electrons in the electromagnetic cascade, were considered point-like. At low energies, the cascade extension can be ignored and the approximation is valid. However, at high energy, this extension is no longer negligible and must be taken into account.

3. As the energy of the cascade increases, the number of photons produced also grows. To reduce the computing power necessary to perform the detector simulation, a merging of the incident photons is carried out, within a time interval of 5 ns. This makes it possible to manage large flows of photons with a very small loss of precision but a computational gain.

As comparison, Figure 4.4 also shows the distribution of charges collected by each DOM, plotted as in the previous figure but for a 10 PeV cascade. The three points explained above are implemented in the simulation. The number of sensors that receive light is significantly greater, and the collected charges are three orders of magnitude higher. The impact of the dust layer remains visible, as does the background noise in the simulation with Event-generator. A noticeable difference in the high-charge DOMs is apparent. A more thoughtful analysis of high energy events and explanation is provided in the following section.

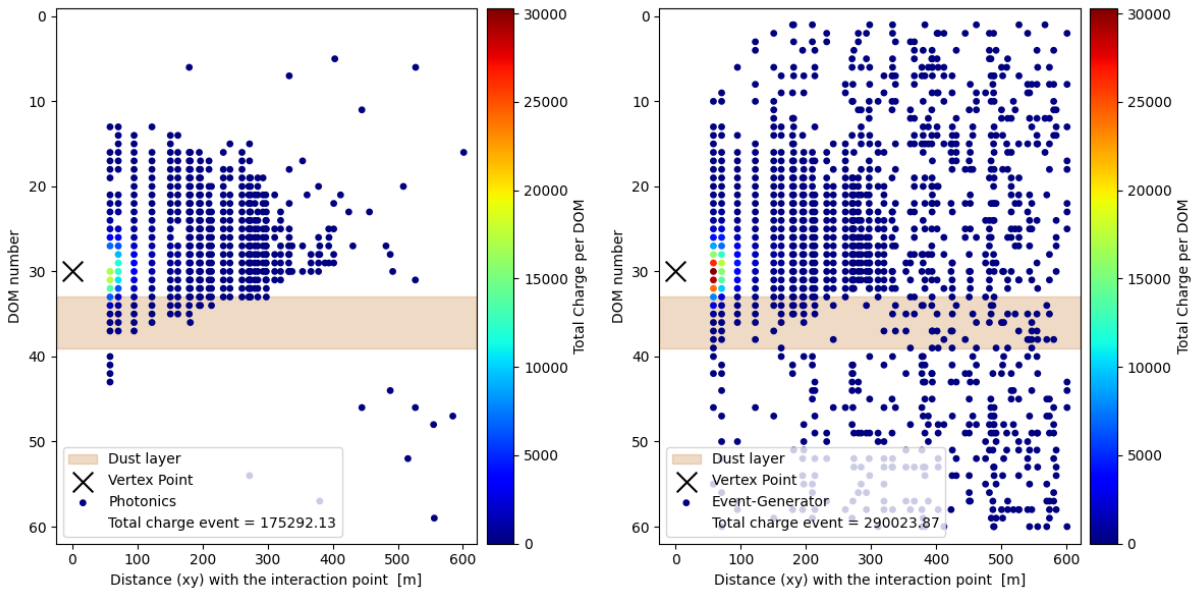

Figure 4.4: Complete simulation of total charge collected by each DOM for a 10 PeV cascade with the vertex at (0,0,0) with Photonics on the left and Event-Generator on the right.

4.2 High energy first comparaison

It is time to study the differences that appears between these two methods for a wide energy and vertex position range. A dataset of 1000 events has been generated following a neutrino spectrum in E^{-1} with energy between $1\ \mathrm{PeV}$ and $1\ \mathrm{EeV}$. The left part of Figure 4.5 shows the energy distribution of these data. Given the semi-logarithmic scale of the graph and the fact that the bins of this histogram are constructed to be constant on a logarithmic scale, the power law is clearly represented by a uniform distribution. The right graph of the same figure displays the distribution of the simulated events withdepth, showing a uniform distribution throughout the detector. The data are presented in the IceCube coordinate system.

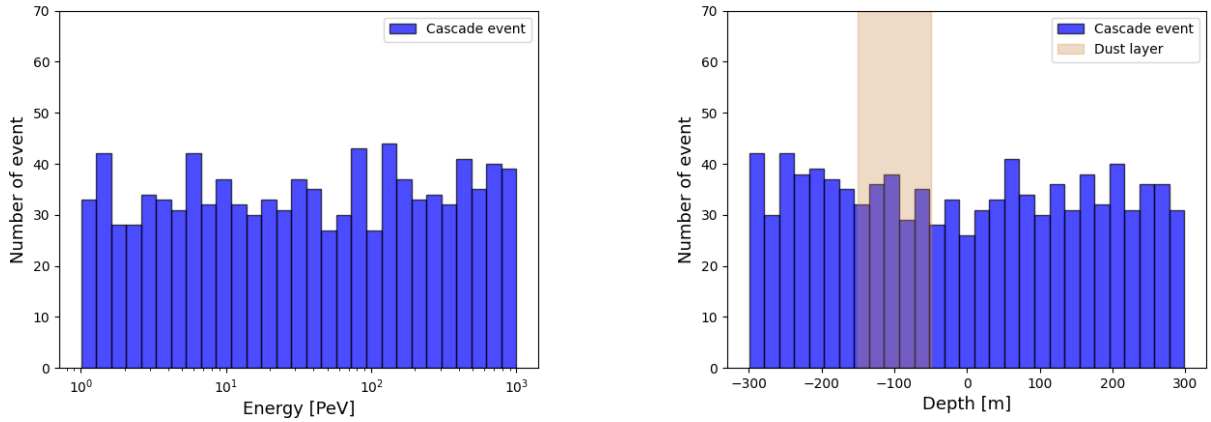

Figure 4.5: Energy distribution on the left and vertex depth distribution on the right for the set of 1000 events with energies ranging from 1 PeV to 1 EeV.

The simulated events exhibit high energies and interact at various depths within the detector. This allows for a comparison between the simulations performed with Photonics and those conducted with Event-generator methods. This comparison is made by analyzing the representative data simulated by each method: the predicted total charge.

First, it is relevant to calculate the total charge collected by each DOM, independently of the others, for each event. A representative event characterized by an extremely high energy, approximately 100 PeV, has been selected. Figure 4.6 therefore shows the distribution of this charge by DOM for each of the methods. In blue, these are the RecoPulses resulting from the injection of MCPulses into DetectorSegment, while in red, these are the RecoPulses produced by the Event-Generator CNN.

Differences are observed on this graph both for low and high collected values. In the first case, Event-generator strongly dominates. This is due to the background noise previously explained. In the second case, fluctuations appear between the two methods, leading to significant discrepancies for certain energy ranges. Photonics presents a peak of DOMs with charges around 10^3 that is not present in the other method, which shows a more regular distribution extending to slightly higher charges, up to 10^4. The total charge recorded by the detector during the event is obtained by summing the charge collected by each DOM. The result of this sum for each method is:

Methods	Total Charge Event	Mean
Photonic	1 497 961.02	1 411.84
Event Generator	3 045 211.96	2 364.30

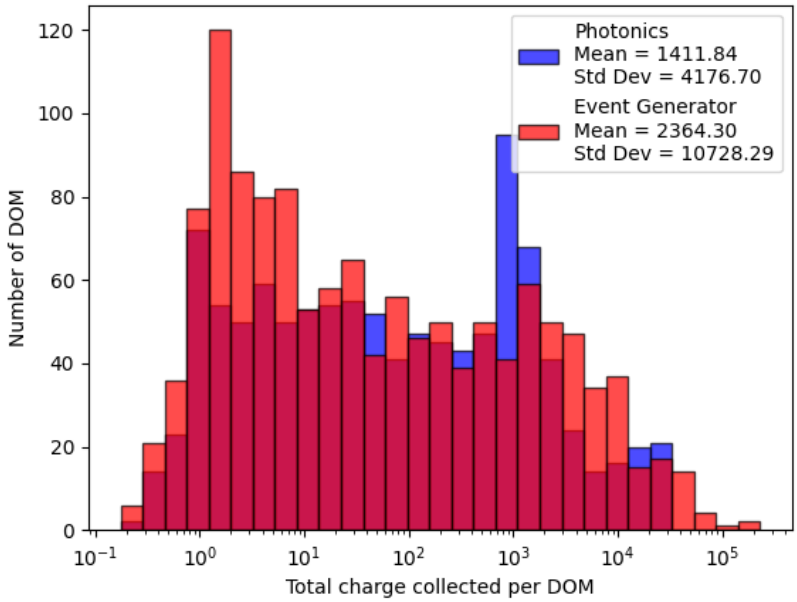

Figure 4.6: Distribution of the total charge collected by each DOM for an event of energy: $E = 100.42$ PeV.

This shows a clear disagreement between the two simulations, with the total charge recorded by Event-Generator being twice as large as the same data predicted by Photonics. The same observation applies for the mean collected charge.

It is therefore interesting to examine the evolution of the total charge per event. Figure 4.7 thus presents the distribution of these values for Photonics in blue and Event-Generator in red.

This figure shows a good agreement between the two simulations up to a charge of approximately 5×10^5. Beyond this value, a clear difference appears between the two simulations. Photonics, inculding the detector simulation, predicts the majority of high-energy events with charges between 10^5 and 2×10^6. The distribution then drops sharply and stops at 5×10^6. Simulations performed with Event-Generator calculate total charges up to 2×10^7. They also show a region with a slight increase between charges of 10^5 and 6×10^6. Consequently, the total charges collected simulated by Event-Generator are much larger than those simulated by Photonics for high-energy events.

An explanation can be provided to account for this difference. The simulations are based on an approximation that states the charge deposited in the detector increases linearly with the energy of the incident particle. This approximation is physically justified up to energies of $\sim 1\text{EeV}$[1]. However, when the electronic response of the detector is taken into account, this linearity at high energy is broken. This is due partly to the saturation of the PMTs receiving too many photons in a very short time, and partly to the analog-to-digital conversion that occurs during signal processing in the DOM.

Given this information, it is important to examine the simulation content in more detail. When using Photonics, the total charge is calculated based on the RecoPulses, i.e., the simulation of the signal arriving at the DOMs, MCPEs, are then processed through DetectorSegment that simulates the saturation of the PMTs and DOMs. This is reflected by the abrupt end of the blue histogram, leading to a clear absence of very high collected charges.

[1] Above these energies, the LPM effect must be considered. Interested readers are referred to [84].

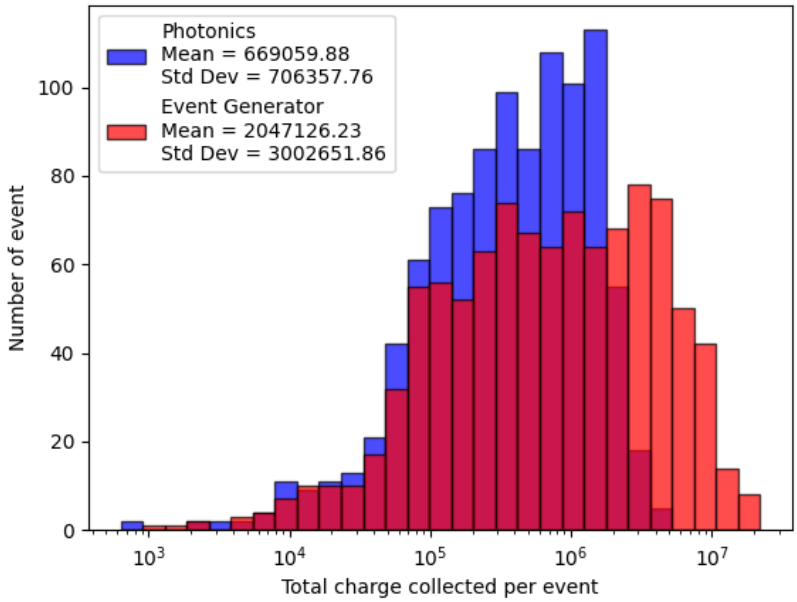

Figure 4.7: Total collected charge distribution per event for a set of 1000 events with energies ranging from 1 PeV *to* 1 EeV.

In the simulation performed with Event-Generator, it is clear that saturation is not taken into account given the particularly high collected charges. This can be explained by the fact that the neural network was initially designed to perform event reconstruction at low energy. It was supposed to take as input the signals from the DOMs, the RecoPulses. This type of data contains certain characteristics of the detector that the NN should be able to reproduce. However, this is not sufficient because the dataset on which the neural network was initially trained contains RecoPulses from low-energy events, for which saturation is not important, and the linear energy scaling is build into the model. Hence, Event Generator cannot simulate saturation effects in the DOMs response.

4.3 Neural Network Retraining

The solution proposed to address this problem is to retrain the neural network to predict the hits of Monte-Carlo photoelectrons at the DOM before involving any further detector response. Ideally, this retraining should be performed and evaluted with high-energy events. However, this requires a large amount of input data. As the computational power and time needed to simulate an event increase drastically with its energy, only a limited number of high and very high energy simulations are available. Therefore, the training cannot be performed on this range of data.

A dataset has been made available[2] in the form of 15,000 .hdf5 and .3 files. These files are suitable for training because they contain both the MCPE hits and the parameters of the events that produce them, allowing the NN to evaluate, via a loss function, the errors it makes.

The training dataset contains 15 900 809 events at a fixed energy of 10 TeV and uniformly distributed throughout the detector volume. It has been divided into three parts as explained in section 3.3.1 and its distribution is presented in the following table:

[2]We warmly thank Alina Kochocki for sharing her simulations.

	Number of events	Percentage
Training	11 025 665	69.34
Validation	2 470 125	15.53
Test	2 405 019	15.13
Total	15 900 809	100

The training requires significant computational power, thus the use of Graphics Processing Units (GPUs) is necessary. These are electronic circuits developed to perform calculations very quickly. Additionally, they have the major advantage of being able to execute the same task simultaneously on multiple datasets, excelling in tasks that require the repetition of the same operation numerous times. This parallelization significantly reduces the training time of the neural network. The computational interface is provided by HTCondor [85], a system that allocates computational resources for complex tasks. It distributes the available power among independent and asynchronous tasks.

The training evaluates the losses that occur when a part of the training dataset is passed through the NN and aims to minimize them. The neural network improves through iterative repetition of these steps. The more repetitions, the better the training, until the point where further gains become negligible. However, since Condor servers are in high demand, a maximum runtime of two days is allowed for each request. This time limit restricts the number of possible training iterations. Using the software TensorBoard [86], it is possible to monitor the evolution of losses during the process to ensure proper training and a sufficient number of repetitions. This is shown in Figure 4.8. The light blue curve represents the losses calculated on the training dataset, while the purple one represents those on the validation dataset.

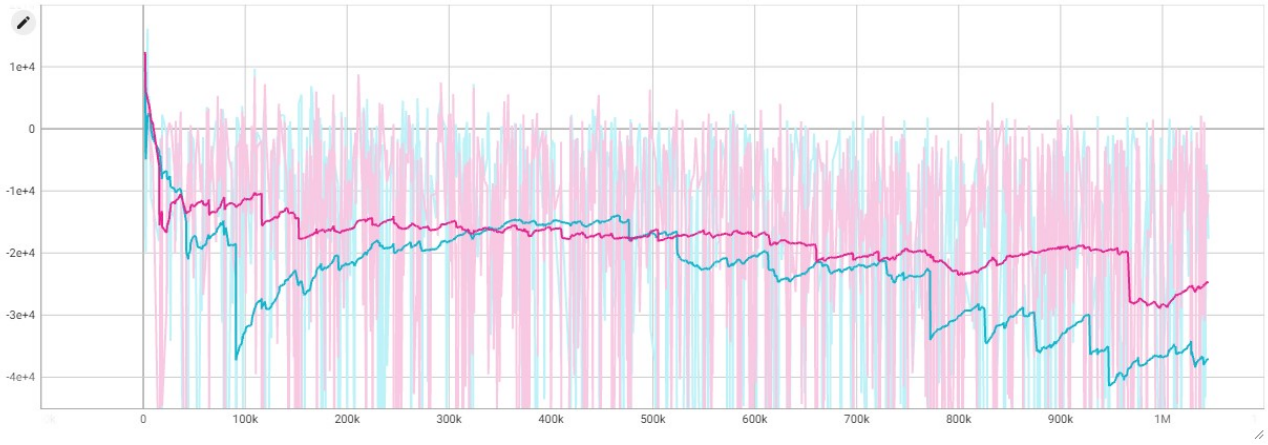

Figure 4.8: Evolution of calculated losses as a function of the number of training iterations.

This figure shows that the training proceeded correctly, as a clear and consistent minimization of losses is visible across both datasets. The total number of steps performed is 1 045 102.

Regarding the neural network's specific feature, another internal change was made. Initially, the number of asymmetric Gaussians used in the loss function was $K = 3$. This value was increased to $K = 10$ to improve training performance. However, this has the consequence of increasing the computational load and thus extending the training time.

4.4 Low energy retraining evaluation

Now that the network has been retrained, its performance needs to be evaluated. This is done using a dataset of 100 000 events uniformly distributed throughout the detector's volume, all with an energy of 10 TeV. It would have been interesting to perform this analysis on a high-energy dataset, but the limited number of high-energy simulations available prevents obtaining representative results. Choosing a larger but lower-energy dataset remains consistent because the NN is trained on MCPEs. These data are simulated based on the approximation that the deposited charge increases linearly with the incident neutrino's energy. Therefore, the results obtained at these lower energies can be extrapolated to higher energies.

Thus, similarly to what was done in subsection 4.2, it is relevant to look again at the total predicted charge per event. The distribution of this value is presented in Figure 4.9 for three different simulation techniques.

This time, in addition to the two previously mentioned methods, the full Monte Carlo simulation is used for comparison. It is the most accurate simulation in terms of the system's physical properties. So, the other two should aim to reach this one.

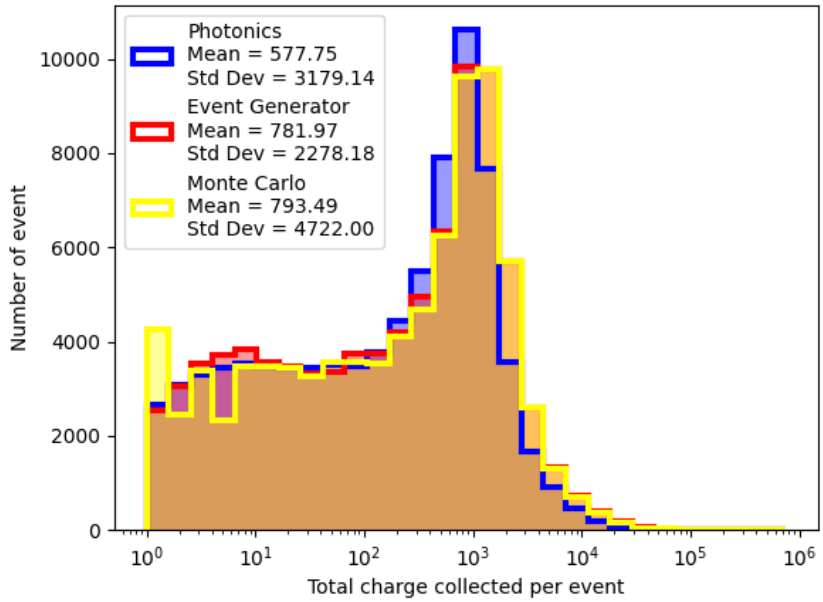

Figure 4.9: Distribution of the total charge collected per event for simulations using Photonics (blue), Event-Generator (red), and full Monte Carlo (yellow).

On this figure, the blue curve represents the values from the Photonics simulation, the red curve represents those from the Event-Generator, and the yellow curve from the Monte Carlo. There is a good consistency among the three simulations. For very low collected charges, Photonics and Event-Generator are close to each other but differ from Monte Carlo. This could be due to statistical fluctuations linked to the data set. Then, for larger charges, the three methods agree, although a discrepancy with Photonics appears, while a particular agreement between the curves from Monte Carlo and Event-Generator can be observed. The histogram from Photonics thus has a peak at slightly lower collected charges. Finally, all three curves drop sharply beyond a charge of 2×10^3 as 10 TeV events can no longer deposit higher charges in the detector, but again, this drop occurs slightly earlier

for Photonics. It thus appears that Event-Generator is capable of more accurately simulating the total charge collected in the detector.

Since all cascades result from an incident 10 TeV neutrino, the total amount of Cherenkov photons produced is approximately the same for all events. However, as the previous figure shows, the charge collected by the detector, and more specifically by the DOMs, varies from one event to another. This variation is due to the propagation of photons in the ice, the detection medium of IceCube, and the position of the interaction itself. Therefore, it is crucial to ensure that the NN has incorporated these detector-specific characteristics during its training.

Since the properties of the ice change with depth, it is relevant to examine the variation in the collected charge as a function of the depth, expressed in IceCube coordinates, of the primary interaction vertex. This is represented in the graph in Figure 4.10, where the curves blue, red, and yellow again represent the simulations performed with Photonics, Event-Generator, and Monte-Carlo, respectively.

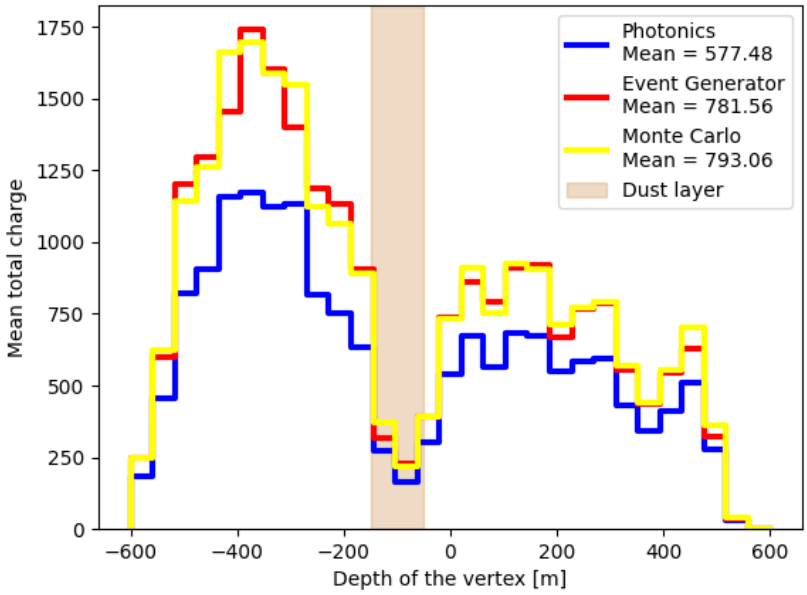

Figure 4.10: Distribution of the total charge collected by the detector as a function of the depth of the primary vertex, expressed in IceCube coordinates.

The obtained distributions are highly asymmetric and non-uniform. This indicates that certain areas of the detector are less conducive to photon propagation. The charge collected from an interaction occurring in these areas is therefore lower, as expected from studies on the ice properties [57]. The prediction from Photonics appears unusually low, while the close proximity of the red and yellow curves is striking. This difference is reflected in the average load calculated with each method, indicated in the legend.

Methods	Mean Total Charge
Photonic	577.48
Event-Generator	781.56
Monte-Carlo	793.06

The reasons for the lower charge predicted by Photonics are unclear and deserve further analysis.

The key point of this analysis is the sharp drop in collected charge at the dust layer. This was expected since the increased presence of dust in this ice layer significantly enhances photon scattering. Consequently, a substantially reduced number of photons reach the detector. This drastic reduction clearly indicates that the internal properties of the detector are well accounted for both Photonics and Monte-Carlo. As Event-Generator also follows this trend, it demonstrates that the NN, through its training, has successfully incorporated these characteristics as well.

Conclusion and outlook

Thanks to the detections made by IceCube, the amount of experimental data on neutrinos increases every day. This is a major advantage because identifying EHE neutrinos involves studying event records over multiple years, thus requiring efficient, robust, and precise analysis methods. With the development of Deep Learning in recent years, the research field of high-energy event analysis is rapidly evolving. The advent of new simulation and reconstruction techniques using neural networks, developed by the IceCube collaboration, is evidence of this.

The goal of neutrino detection simulations is to accurately reproduce the Cherenkov light produced by secondary particles resulting from neutrino interaction in ice, propagate this light, and predict the detector response. This simulation is carried out in several stages, one of the most important being the prediction of the temporal distribution and the number of photons reaching each optical module. This work has tested the validity of using one of these new reconstruction methods, based on a convolutional neural network and named Event-Generator, to simulate this distribution for cascade events.

An initial study of the total charge collected per event of very high energy events indicated that the method, originally developed for reconstruction, could not be applied for these applications without changes. To obtain these results, the predictions of Event-Generator were compared to those of a simulation technique that has been used for several years, Photonics. A retraining of the neural network, using a different type of data, was therefore conducted to improve its ability to account for specific detector characteristics, such as saturation. Finally, a second evaluation was performed on the retrained model using a low-energy data set. This time, the full Monte Carlo simulation was added. Closer to reality but requiring more computational power, this method helped demonstrate the success of the CNN to predict the total charge collected per event and the attenuation due to the dust layer in its simulation of the PDFs.

There are multiple possibilities for improvements. The most prominent one is currently to perform a new training by including variations of the Ice model, and thus the properties of the ice, in the input dataset. This would certainly allow to simulate events with arbitrary ice properties, a skill extremely valuable for neutrino searches! On a smaller scale, it would now be interesting to perform various training types by changing hyper-parameter such as the loss function to find the most suitable ones. These topics unfortunately could not be covered in this master's thesis and are therefore left for future research projects.

Summarizing from the beginning, this research work within the IceCube Collaboration began with familiarization with the IceCube Core software, where all simulations were conducted, and with the data format processed within it. This was achieved by studying the existing simulations. A feasibility evaluation was then performed through an initial comparison between the two main methods employed: Event-Generator and Photonics. This comparison was conducted on a set of high-energy

data specifically simulated for this purpose. Finally, given the results of this stage of the research, a retraining of the neural network was performed using the appropriate type of data. This allowed the completion of this Master's thesis by comparing this retraining with, this time, the Photonics and full Monte Carlo methods.

Bibliography

[1] Abbott, B. P., Abbott, R., Adhikari, R., Ajith, P., Allen, B., Allen, G., Amin, R. S., Anderson, S. B., Anderson, W. G., Arain, M. A., Araya, M., Armandula, H., Armor, P., Aso, Y., Aston, S., Aufmuth, P., Aulbert, C., Babak, S., Baker, P.,. . . Daw, E. J. (2009). LIGO : the Laser Interferometer Gravitational-Wave Observatory. *Reports On Progress In Physics, 72(7), 076901.* https://doi.org/10.1088/0034-4885/72/7/076901

[2] Accadia, T., Acernese, F., Alshourbagy, M., Amico, P., Antonucci, F., Aoudia, S., Arnaud, N., Arnault, C., Arun, K. G., Astone, P., Avino, S., Babusci, D., Ballardin, G., Barone, F., Barrand, G., Barsotti, L., Barsuglia, M., Basti, A., Bauer, T. S.,. . . Del Prete, M. (2012). Virgo : a laser interferometer to detect gravitational waves. *Journal Of Instrumentation, 7(03), P03012.* https://doi.org/10.1088/1748-0221/7/03/p03012

[3] Aartsen, M., Ackermann, M., Adams, J., Aguilar, J., Ahlers, M., Ahrens, M., Altmann, D., Andeen, K., Anderson, T., Ansseau, I., Anton, G., Archinger, M., Argüelles, C., Auer, R., Auffenberg, J., Axani, S., Baccus, J., Bai, X., Barnet, S.,. . . Fuchs, T. (2017). The IceCube Neutrino Observatory: Instrumentation and Online Systems. *Journal Of Instrumentation, 12(03), P03012.* https://doi.org/10.1088/1748-0221/12/03/p03012

[4] Ageron, M., Aguilar, J., Samarai, I. A., Albert, A., Ameli, F., André, M., Anghinolfi, M., Anton, G., Anvar, S., Ardid, M., Arnaud, K., Aslanides, E., Jesus, A. A., Astraatmadja, T., Aubert, J., Auer, R., Barbarito, E., Baret, B., Basa, S.,. . . Fiorello, C. (2011). ANTARES : The first undersea neutrino telescope. *Nuclear Instruments And Methods In Physics Research. Section A, Accelerators, Spectrometers, Detectors And Associated Equipment, 656(1), 11-38.* https://doi.org/10.1016/j.nima.2011.06.103

[5] Abreu, P., Aglietta, M., Ahn, E., Allard, D., Allekotte, I., Allen, J., Castillo, J. A., Alvarez-Muñiz, J., Ambrosio, M., Aminaei, A., Anchordoqui, L., Andringa, S., Antičić, T., Anzalone, A., Aramo, C., Arganda, E., Arisaka, K., Arqueros, F., Asorey, H.,. . . De Mello, W., Junior. (2011). The exposure of the hybrid detector of the Pierre Auger Observatory. *Astroparticle Physics, 34(6), 368-381.* https://doi.org/10.1016/j.astropartphys.2010.10.001

[6] Michelson, P. F., Atwood, W. B., & Ritz, S. (2010). Fermi Gamma-ray Space Telescope : high-energy results from the first year. *Reports On Progress In Physics, 73(7), 074901.* https://doi.org/10.1088/0034-4885/73/7/074901

[7] Aartsen, M. G., Ackermann, M., Adams, J., Aguilar, J. A., Ahlers, M., Ahrens, M., Altmann, D., Anderson, T., Arguelles, C., Arlen, T. C., Auffenberg, J., Bai, X., Barwick, S. W., Baum, V., Beatty, J. J., Tjus, J. B., Becker, K., BenZvi, S., Berghaus, P.,. . . Hallgren, A. (2014).

Observation of High-Energy Astrophysical Neutrinos in Three Years of IceCube Data. *Physical Review Letters, 113(10).* https://doi.org/10.1103/physrevlett.113.101101

[8] Aartsen, M., Ackermann, M., Adams, J., Aguilar, J. A., Ahlers, M., Ahrens, M., Samarai, I. A., Altmann, D., Andeen, K., Anderson, T., Ansseau, I., Anton, G., Argüelles, C., Arsioli, B., Auffenberg, J., Axani, S., Bagherpour, H., Bai, X., Barron, J.,. . . Gluesenkamp, T. (2018). Neutrino emission from the direction of the blazar TXS 0506+056 prior to the IceCube-170922A alert. *Science, 361(6398), 147-151.* https://doi.org/10.1126/science.aat2890

[9] Abbasi, R., Ackermann, M., Adams, J., Aguilar, J. A., Ahlers, M., Ahrens, M., Alameddine, J. M., Alispach, C., Alves, A. A., Amin, N. M., Andeen, K., Anderson, T., Anton, G., Argüelles, C., Ashida, Y., Axani, S., Bai, X., Balagopal, A., V., Barbano, A.,. . . Fienberg, A. T. (2022). Evidence for neutrino emission from the nearby active galaxy NGC 1068. *Science, 378(6619), 538-543.* https://doi.org/10.1126/science.abg3395

[10] Abbasi, R., Ackermann, M., Adams, J., Aguilar, J. A., Ahlers, M., Ahrens, M., Alameddine, J. M., Alves, A. A., Amin, N. M., Andeen, K., Anderson, T., Anton, G., Argüelles, C., Ashida, Y., Athanasiadou, S., Axani, S., Bai, X., Balagopal, A., V., Barwick, S. W.,. . . Fischer, L. (2023). Observation of high-energy neutrinos from the Galactic plane. *Science, 380(6652), 1338-1343.* https://doi.org/10.1126/science.adc9818

[11] Huennefeld, M., et al. Combining Maximum-Likelihood with Deep Learning for Event Reconstruction in IceCube. *Proceedings of 37th International Cosmic Ray Conference — PoS(ICRC2021), Sissa Medialab, 2021, p. 1065.*, https://doi.org/10.22323/1.395.1065.

[12] Lundberg, J., Miočinović, P., Woschnagg, K., Burgess, T., Adams, J., Hundertmark, S., Desiati, P., & Niessen, P. (2007). Light tracking through ice and water—Scattering and absorption in heterogeneous media with Photonics. *Nuclear Instruments And Methods In Physics Research. Section A, Accelerators, Spectrometers, Detectors And Associated Equipment, 581(3), 619-631.* https://doi.org/10.1016/j.nima.2007.07.143

[13] Pinkau, K. (2009). History of gamma-ray telescopes and astronomy. *Experimental Astronomy, 25(1-3), 157-171.* https://doi.org/10.1007/s10686-009-9143-z

[14] Abbott, B. P., Abbott, R., Abbott, T. D., Abernathy, M. R., Acernese, F., Ackley, K., Adams, C., Adams, T., Addesso, P., Adhikari, R. X., Adya, V. B., Affeldt, C., Agathos, M., Agatsuma, K., Aggarwal, N., Aguiar, O. D., Aiello, L., Ain, A., Ajith, P.,. . . Bond, C. (2016). Observation of Gravitational Waves from a Binary Black Hole Merger. *Physical Review Letters (Print), 116(6).* https://doi.org/10.1103/physrevlett.116.061102

[15] Pauli, W. (2000). Wissenschaftlicher Briefwechsel Mit Bohr, Einstein, Heisenberg, Letter 259. *Pauli Letter Collection : Letter to Lise Meitner.* https://cds.cern.ch/record/83282/files/meitner_0393.pdf

[16] CERN. (2024, 3 avril). Cosmic rays : particles from outer space. https://home.cern/science/physics/cosmic-rays-particles-outer-space

[17] Diehl, R. (2009b). Particle acceleration in cosmic sites. The European *Physical Journal. D, Atomic, Molecular And Optical Physics, 55(2), 509-518.* https://doi.org/10.1140/epjd/e2009-00183-8

[18] Siming, L. (2019). On the Supernova-remnant Origin of Galactic Cosmic Rays. *BCAS, Vol.33 No.3, 157-163.* https://english.cas.cn/bcas/No3_2019/202001/P020200123484846848345.pdf

[19] Greisen, K. (1966). End to the Cosmic-Ray Spectrum ? *Physical Review Letters (Print), 16(17), 748-750.* https://doi.org/10.1103/physrevlett.16.748

[20] Zatsepin, G., & Kuzmin, V. (1966). Upper limit of the spectrum of cosmic rays. *Journal Of Theoretical Physics Letters, 4, 114-117.* https://courses.physics.illinois.edu/phys596/fa2013/StudentWork/Team3_Final.pdf

[21] Meures, T. (2014). *Development of a sub-glacial array of radio antennas for the detection of the flux of GZK neutrinos* [These de doctorat, Interuniversity Institute for High Energies (ULB - VUB)]. https://iihe.ac.be/sites/default/files/thesis-thomas-meures-phd-2014pdf/thesis-thomas-meures-phd-2014.pdf

[22] Andersen, K. K., & Klein, S. R. (2011). High energy cosmic-ray interactions with particles from the Sun. *Physical Review. D. Particles, Fields, Gravitation, And Cosmology, 83(10).* https://doi.org/10.1103/physrevd.83.103519

[23] Stanev, T. (2010). *High energy cosmic rays*. Springer Science & Business Media.

[24] Grupen, C. (2005). *Astroparticle Physics* (1re éd.). Dans Springer eBooks. https://doi.org/10.1007/3-540-27670-x

[25] Aguilar, J. A.. (2024). PHYS-F467 - Astroparticle physics: *Lecture Cosmic Rays in the Atmosphere* [notes de cours]. IIHE, Université libre de Bruxelles.

[26] Funk, S. (2015). Space- and Ground-Based Gamma-Ray Astrophysics. *arXiv:1508.05190.* https://doi.org/10.1146/annurev-nucl-102014-022036

[27] Kachelrieß, M. K. (s.d.). Lecture Notes on High Energy Cosmic Rays [Lecture Notes]. 17.th Jyväsklyä Summer School, Jyväskylä, Finlande. https://arxiv.org/pdf/0801.4376.pdf

[28] Oikonomou, F. (2022). High-energy neutrino emission from blazars. *Proceedings Of 37th International Cosmic Ray Conference — PoS(ICRC2021).* https://doi.org/10.22323/1.395.0030

[29] Biteau, J., & Meyer, M. (2022). Gamma-Ray Cosmology and Tests of Fundamental Physics. *Galaxies, 10(2), 39.* https://doi.org/10.3390/galaxies10020039

[30] Abbott, B. P., Abbott, R., Abbott, T. D., Abernathy, M. R., Acernese, F., Ackley, K., Adams, C., Adams, T., Addesso, P., Adhikari, R. X., Adya, V. B., Affeldt, C., Agathos, M., Agatsuma, K., Aggarwal, N., Aguiar, O. D., Aiello, L., Ain, A., Ajith, P.,. . . Bond, C. (2016b). Observation of Gravitational Waves from a Binary Black Hole Merger. *Physical Review Letters, 116(6).* https://doi.org/10.1103/physrevlett.116.061102

[31] Speziale, S. (s.d.). Brief introduction to gravitational waves : theory, production and detection [Lecture Notes]. Aix Marseille Univ., Univ. De Toulon, CNRS, CPT, UMR 7332, 13288 Marseille, France. https://indico.in2p3.fr/event/25990/contributions/104569/attachments/72061/115346/GW%20MaNiTou%20Lecture%20Notes.pdf

[32] Branchesi, M. (2016). Multi-messenger astronomy : gravitational waves, neutrinos, photons, and cosmic rays. *Journal Of Physics : Conference Series, 718, 022004.* https://doi.org/10.1088/1742-6596/718/2/022004

[33] Abbott, B. P., Abbott, R., Abbott, T. D., Acernese, F., Ackley, K., Adams, C., Adams, T., Addesso, P., Adhikari, R. X., Adya, V. B., Affeldt, C., Afrough, M., Agarwal, B., Agathos, M., Agatsuma, K., Aggarwal, N., Aguiar, O. D., Aiello, L., Ain, A.,. . . Biwer, C. (2017). Gravitational Waves and Gamma-Rays from a Binary Neutron Star Merger : GW170817 and GRB 170817A. *The Astrophysical Journal. Letters, 848(2), L13.* https://doi.org/10.3847/2041-8213/aa920c

[34] Katz, U. F., & Spiering, C. (2012). High-energy neutrino astrophysics : Status and perspectives. *Progress In Particle And Nuclear Physics, 67(3), 651-704.* https://doi.org/10.1016/j.ppnp.2011.12.001

[35] Mészáros, P. (2017). Astrophysical Sources of High-Energy Neutrinos in the IceCube Era. *Annual Review Of Nuclear And Particle Science, 67(1), 45-67.* https://doi.org/10.1146/annurev-nucl-101916-123304

[36] Murase, K. (2017). *Active Galactic Nuclei as High-Energy Neutrino Sources*. WORLD SCIENTIFIC eBooks (p. 15-31). https://doi.org/10.1142/9789814759410_0002

[37] Stenger V. J. (1992) High Energy Neutrino Astrophysics: Potential Sources and their Underwater Detection. Recueil inédit, Departement of Physics and Astronomy, University of Hawaii Honolulu. https://www.phys.hawaii.edu/~dumand/post/dumandexternal/1992/HDC-12-92.pdf

[38] Aartsen, M. G., Abbasi, R., Ackermann, M., Adams, J. H., Aguilar, J. A., Ahlers, M., Ahrens, M., Alispach, C. M., Amin, N. M. B., Andeen, K., Anderson, W. G., Ansseau, I., Anton, G., Argüelles, C., Auffenberg, J., Axani, S., Bagherpour, H., Bai, X., Barbano, A. M.,. . . Gaisser, T. K. (2021). Detection of a particle shower at the Glashow resonance with IceCube. *Nature, 591(7849), 220-224.* https://doi.org/10.1038/s41586-021-03256-1

[39] Stasto, A. (2003). Ultrahight Energy Neutrino Physics. *International Journal Of Modern Physics A, 19(03), 317-340.* https://doi.org/10.1142/s0217751x04017082

[40] Formaggio, J. A., & Zeller, G. P. (2012). From eV to EeV : Neutrino cross sections across energy scales. *Reviews Of Modern Physics, 84(3), 1307-1341.* https://doi.org/10.1103/revmodphys.84.1307

[41] Chen, Chien-Yi, et al. (2014). Standard Model Explanation of the Ultra-high Energy Neutrino Events at IceCube. *Physical Review D, vol. 89(3), 033012.* https://doi.org/10.1103/PhysRevD.89.033012

[42] Barwick, S. W., & Glaser, C. (2023). *Radio Detection of High Energy Neutrinos in Ice*. WORLD SCIENTIFIC eBooks (p. 237-302). https://doi.org/10.1142/9789811282645_0006

[43] Van Santen, J. (2010). *Markov-Chain Monte-Carlo Reconstruction for cascade-like events in IceCube* [Master-thesis]. Humboldt-Universität zu Berlin. https://user-web.icecube.wisc.edu/~jvansanten/lit/jvs_diplom.pdf

[44] Kowalski M., (2002, August 12) On the cerenkov light emission of hadronic and electromagnetic cascades. DESY-Zeuthen. [internal-note]

[45] Karle, A. (2007). IceCube - Construction Status and Performance Results of the 22 String Detector. *30th international cosmic rays conference, 4, 835-838.* https://bib-pubdb1.desy.de/record/83502/export/hr

[46] Yu, S. (2023). Measurement of Atmospheric Muon Neutrino Disappearance Using CNN Reconstructions with IceCube. *Phys. Sci. Forum 2023, 8(1), 62.* https://doi.org/10.3390/psf2023008062

[47] Stokstad, R. (s.d.). Design and Performance of the IceCube Electronics. IceCube Collaboration. [internal-note] https://cds.cern.ch/record/920022/files/p20.pdf

[48] Yuan, T. (2023). Detecting neutrinos in IceCube with Cherenkov light in the South Pole ice. *Nuclear Instruments And Methods In Physics Research. Section A, Accelerators, Spectrometers, Detectors And Associated Equipment, 1054, 168440.* https://doi.org/10.1016/j.nima.2023.168440

[49] Karle, A. (2009). IceCube. *PROCEEDINGS OF 31st ICRC, ŁÓDŹ.* https://doi.org/10.22323/1.196.0053

[50] Abbasi, R., Abdou, Y., Abu-Zayyad, T., Ackermann, M., Adams, J., Aguilar, J. A., Ahlers, M., Allen, M., Altmann, D., Andeen, K., Auffenberg, J., Bai, X., Baker, M. D., Barwick, S. W., Bay, R., Alba, J. L. B., Beattie, K., Beatty, J. J., Bechet, S.,. . . Hanson, K. (2012). The design and performance of IceCube DeepCore. *Astroparticle Physics, 35(10), 615-624.* https://doi.org/10.1016/j.astropartphys.2012.01.004

[51] Abbasi, R., Abdou, Y., Ackermann, M., Adams, J., Aguilar, J. A., Ahlers, M., Altmann, D., Andeen, K., Auffenberg, J., Bai, X., Baker, M. D., Barwick, S. W., Baum, V., Bay, R., Beattie, K., Beatty, J. J., Bechet, S., Tjus, J. B., Becker, K.,. . . Halzen, F. (2013). IceTop : The surface component of IceCube. *Nuclear Instruments And Methods In Physics Research. Section A, Accelerators, Spectrometers, Detectors And Associated Equipment, 700, 188-220.* https://doi.org/10.1016/j.nima.2012.10.067

[52] DuVernois M., The IceCube Upgrade. [slides]. University of Wisconsin-Madison. https://indico.fnal.gov/event/22303/contributions/245856/attachments/157629/206323/duvernois_icecube_upgrade.pdf

[53] IceCube Docs. (2024, 9 mai). icetray(328e9b87) - Dataclasses documentation - Coordinate Systems. https://docs.icecube.aq/icetray/main/projects/dataclasses/coordinates.html

[54] FRANK I., TAMM Ig. (1937). coherent visible radiation of fast electrons passing through matter. *C. R. Sc. U.R.S.S., 3, (14), 109-114*

[55] Quand les particules chargées dépassent la vitesse de la lumière - l'effet Tcherenkov - la découverte, ses applications et son découvreur. (2012, 24 mars). IN2P3 Events Directory (Indico). https://indico.in2p3.fr/event/6320/

[56] Cherenkov radiation detected in 2D regime. (2024, 9 mai). Internet. https://www.resonancescience.org/blog/cherenkov-radiation-detected-in-2d-regime

[57] Aartsen, M. G. & IceCube Collaboration. (2013). Measurement of South Pole ice transparency with the IceCube LED calibration system. *Nuclear Instruments and Methods in Physics Research A, 711, 73–89.* https://pdf.sciencedirectassets.com/271580/1-s2.0-S0168900213X00075/1-s2.0-S0168900213001460/main.pdf

[58] Mikkelsen, R. E., Poulsen, T., Uggerhøj, U. I., & Klein, S. R. (2016). Characteristics of Cherenkov radiation in naturally occurring ice. *Physical Review. D/Physical Review. D., 93(5).* https://doi.org/10.1103/physrevd.93.053006

[59] Detecting Neutrinos (2024, 26 mai). IceCube Masterclass. https://masterclass.icecube.wisc.edu/en/learn/detecting-neutrinos

[60] Ahlers, M., Helbing, K., & De Los Heros, C. P. (2018). Probing particle physics with IceCube. *European Physical Journal. C, Particles And Fields, 78(11).* https://doi.org/10.1140/epjc/s10052-018-6369-9

[61] Aartsen, M. G., Abbasi, R., Abdou, Y., Ackermann, M., Adams, J. H., Aguilar, J. A., Ahlers, M., Altmann, D., Auffenberg, J., Bai, X., Baker, M., Barwick, S. W., Baum, V., Bay, R., Beatty, J. J., Bechet, S., Tjus, J. B., Becker, K. H., Benabderrahmane, M. L.,. . . Grandmont, D. T. (2013). Evidence for High-Energy Extraterrestrial Neutrinos at the IceCube Detector. *Science, 342(6161).* https://doi.org/10.1126/science.1242856

[62] IceCube Docs (2024, 9 mai). icetray(328e9b87) - Q Frames. https://software.icecube.wisc.edu/icetray/main/projects/icetray/qframes.html

[63] IceCube Docs (2024, 9 mai). icetray(328e9b87) - i3frame. https://docs.icecube.aq/icetray/main/projects/icetray/classes/i3frame.html

[64] Abbasi, R., Ackermann, M., Adams, J., Aguilar, J., Ahlers, M., Ahrens, M., Alispach, C., Alves, A., Amin, N., An, R., Andeen, K., Anderson, T., Ansseau, I., Anton, G., Argüelles, C., Axani, S., Bai, X., Balagopal, A., V., Barbano, A.,. . . Gallagher, J. (2021b). A convolutional neural network based cascade reconstruction for the IceCube Neutrino Observatory. *Journal Of Instrumentation, 16(07), P07041.* https://doi.org/10.1088/1748-0221/16/07/p07041

[65] Aartsen, M. G., Abbasi, R., Ackermann, M., Adams, J., Aguilar, J. A., Ahlers, M., Altmann, D., Arguelles, C., Auffenberg, J., Bai, X., Baker, M., Barwick, S. W., Baum, V., Bay, R., Beatty, J. J., Tjus, J. B., Becker, K.-., BenZvi, S., Berghaus, P.,. . . Hanson, K. (2014). Energy reconstruction methods in the IceCube neutrino telescope. *Journal Of Instrumentation, 9(03), P03009.* https://doi.org/10.1088/1748-0221/9/03/p03009

[66] IceCube Docs (2024, 9 mai). icetray(328e9b87) - overview. https://software.icecube.wisc.edu/icetray/main/info/overview.html

[67] Carlos Díaz-Vélez, J. (2020, juin). Neutrino and Air Shower Simulations in IceCube [Diapositives]. IceCube Bootcamp, Madison, Wisconsin. https://events.icecube.wisc.edu/event/123/contributions/6472/attachments/5487/6310/Simulation_in_IceCube_2020.pdf

[68] Heck, D., Knapp, J., Capdevielle, J., Schatz, G., & Thouw, T. (n.d.). CORSIKA: A Monte Carlo code to simulate extensive air showers. *INSPIRE*. https://inspirehep.net/literature/469835

[69] Carminati, G., Bazzotti, M., Margiotta, A., & Spurio, M. (2008). Atmospheric MUons from PArametric formulas : a fast GEnerator for neutrino telescopes (MUPAGE). *Computer Physics Communications, 179(12), 915-923*. https://doi.org/10.1016/j.cpc.2008.07.014

[70] IceCube Docs (2024, 9 mai). icetray(328e9b87) - neutrino-generator. https://docs.icecube.aq/icetray/main/projects/neutrino-generator/intro.html

[71] Abbasi, R., Ackermann, M., Adams, J., Aguilar, J. A., Ahlers, M., Ahrens, M., Alispach, C. M., Alves, A. A., Amin, N. M. B., An, R., Andeen, K., Anderson, T., Ansseau, I., Anton, G., Argüelles, C., Axani, S., Bai, X., Balagopal, A., Barbano, A. M.,. . . Gallagher, J. (2021). LeptonInjector and LeptonWeighter : A neutrino event generator and weighter for neutrino observatories. *Computer Physics Communications, 266, 108018*. https://doi.org/10.1016/j.cpc.2021.108018

[72] Koehne, J., Frantzen, K., Schmitz, M., Fuchs, T., Rhode, W., Chirkin, D., & Tjus, J. B. (2013). PROPOSAL : A tool for propagation of charged leptons. *Computer Physics Communications, 184(9), 2070-2090*. https://doi.org/10.1016/j.cpc.2013.04.001

[73] IceCube Docs (2024, 24 mai). icetray(328e9b87) - I3Particle. https://docs.icecube.aq/icetray/main/projects/dataclasses/particle.html

[74] IceCube Docs (2024, 24 mai). icetray(328e9b87) - clsim - overview. https://docs.icecube.aq/icetray/main/projects/clsim/overview.html

[75] IceCube Docs (2024, 24 mai). icetray(328e9b87) - Photon Propagation Code (ppc). https://docs.icecube.aq/icetray/main/projects/ppc/

[76] IceCube Docs (2024, 24 mai). icetray(328e9b87) - DOMLauncher Project - PMTResponseSimulator. https://docs.icecube.aq/icetray/main/projects/DOMLauncher/PMTRes.html

[77] Larson, M. J. (2013). *Simulation and Identification of non-poissonian Noise Triggers in the IceCube Neutrino Detector*, [These de doctorat, The University of Alabama]. https://inspirehep.net/files/147e9132d1d0245895dc407c4dd7505f

[78] IceCube Docs (2024, 24 mai). icetray(328e9b87) - DOMLauncher Project - DOMLauncher Project. https://docs.icecube.aq/icetray/main/projects/DOMLauncher/DOML.html

[79] Hünnefeld, M. (2017). *Online Reconstruction of Muon-Neutrino Events in IceCube using Deep Learning Techniques* [Master Thesis]. Technische Universität Dortmund.

[80] Neural network activation function. (2024, 20 mai). A new activation function for Neural Networks - logmoid. https://www.linkedin.com/pulse/activation-functions-neural-networks-leonardo-calderon-j-

[81] Nunes da Silva I., Spatti D., Flauzino R. A., Bartocci Liboni L., dos Reis Alves S.F. (2017). *Artificial Neural Networks: a practical course.* Springer International Publishing. https://doi.org/10.1007/978-3-319-43162-8

[82] Kromydas, B., & Kromydas, B. (2024, February 5). Training neural networks for beginners. LearnOpenCV – Learn OpenCV, PyTorch, Keras, Tensorflow With Code, & Tutorials. https://learnopencv.com/how-to-train-neural-networks-for-beginners/

[83] Aartsen, M., Ackermann, M., Adams, J., Aguilar, J., Ahlers, M., Ahrens, M., Alispach, C., Andeen, K., Anderson, T., Ansseau, I., Anton, G., Argüelles, C., Auffenberg, J., Axani, S., Backes, P., Bagherpour, H., Bai, X., Balagopal, A., V., Barbano, A.,. . . Glauch, T. (2020). In-situ calibration of the single-photoelectron charge response of the IceCube photomultiplier tubes. *Journal Of Instrumentation, 15(06), P06032.* https://doi.org/10.1088/1748-0221/15/06/p06032

[84] Alvarez-Muñiz, J., & Zas, E. (1998). The LPM effect for EeV hadronic showers in ice : implications for radio detection of neutrinos. *Physics Letters. B, 434(3-4), 396-406.* https://doi.org/10.1016/s0370-2693(98)00905-8

[85] HtCondor user guide. (2024, 10 juin) Internet. https://htcondor.readthedocs.io/en/latest/users-manual/quick-start-guide.html

[86] Tensorboard references. (2024, 10 juin) Internet. https://github.com/tensorflow/tensorboard/blob/master/README.md